Geomechanics for Energy and the Environment 48 (2026) 100926

Contents lists available at ScienceDirect

Geomechanics for Energy and the Environment

journal homepage: www.elsevier.com/locate/gete

Stratigraphic-interface controls on injection-induced Coulomb loading in layered reservoir systems

Shu-Gang Ai [a], Ke Gao [a,b,*]

[a] Department of Earth and Space Sciences, Southern University of Science and Technology, Shenzhen, Guangdong 518055, China
[b] Guangdong Provincial Key Laboratory of Geophysical High-resolution Imaging Technology, Department of Earth and Space Sciences, Southern University of Science and Technology, Shenzhen, Guangdong 518055, China

ARTICLE INFO

Keywords:
Subsurface fluid injection
Layered reservoirs
Stratigraphic interfaces
Poroelastic stress transfer
Injection-induced Coulomb loading

ABSTRACT

Subsurface fluid injection for geothermal energy, carbon storage and wastewater disposal often occurs in layered systems where faults intersect reservoir–caprock and reservoir–basement interfaces. These contacts are commonly treated as passive boundaries, although they can alter pressure diffusion, poroelastic stress transfer and slip tendency. We model them as finite-thickness hydro-mechanical zones in a representative caprock–reservoir–basement system containing a reservoir-crossing fault, solving the Biot poroelastic equations and evaluating the Coulomb failure stress change and a Dieterich-type relative seismicity-rate indicator on the interfaces and the fault. The rate results are diagnostic indicators of loading tendency, not simulations of spontaneous slip, rupture propagation or frictional weakening. Three equal-mass injection protocols (10, 30 and 90 days) and an end-member transmissivity-growth scenario are compared. For intact interfaces, short high-rate injection produces the largest near-well loading pulse but the most localized footprint, whereas longer injection reduces peak pressure while extending positive Coulomb loading after shut-in. The reservoir–basement contact carries the broader loading footprint while the reservoir–caprock contact carries the larger local shear-stress change; control experiments show this asymmetry is not caused by the stiffness contrast. Prescribed transmissivity growth drains pressure near the injector but focuses Coulomb loading at fault-interface intersections. The relative rate indicator is reported as a function of the background stress state of each surface; these results are diagnostic measures of time-dependent loading persistence and do not forecast earthquake occurrence, magnitude or rate.

Introduction

Subsurface fluid injection is widely used in geothermal energy development, geological carbon storage, wastewater disposal, hydrocarbon reservoir stimulation and underground energy storage. These operations can perturb pore pressure and in situ stress, leading to concerns about induced seismicity, subsurface deformation, and the long-term integrity of engineered geological systems.[1–5] These concerns are particularly relevant in stratified geological formations, where caprocks, interbeds, basement units, and laterally continuous lithological contacts can control pressure diffusion, stress redistribution, and potential slip localization.[6–9] In such settings, injection-induced pressure buildup and stress changes are governed not only by operational parameters, including injection rate, cumulative injected volume, and well pressure, but also by geological architecture, especially permeability and stiffness contrasts, sealing layers, stratigraphic contacts, and pre-existing faults.[10–13] Therefore, assessing injection-induced instability in layered reservoirs requires consideration of both injection conditions and geological architecture, which together determine the timing, location, and persistence of pressure- and stress-driven destabilization.

Among the geological structures involved in injection-induced instability, pre-existing faults have received the most attention. Fault reactivation is commonly interpreted through the combined effects of pore-pressure diffusion and poroelastic stress transfer. Elevated pore pressure reduces the effective normal stress on hydraulically connected faults, whereas poroelastic deformation can perturb Coulomb stress outside the main pressure plume.[10,11,13–15] Field observations and hydromechanical analyses show that fault instability and induced seismicity cannot be explained by pore-pressure diffusion alone, because poroelastic stress changes, fault hydraulic properties, connectivity,

* Corresponding author at: Department of Earth and Space Sciences, Southern University of Science and Technology, Shenzhen, Guangdong 518055, China.
E-mail addresses: aisg@sustech.edu.cn (S.-G. Ai), gaok@sustech.edu.cn (K. Gao).

https://doi.org/10.1016/j.gete.2026.100926
Received 22 June 2026; Received in revised form 21 October 2026; Accepted 24 October 2026
Available online 4 November 2026
2352-3808/© 2026 Elsevier Ltd. All rights are reserved, including those for text and data mining, AI training, and similar technologies.

geometry, and aseismic slip can all influence how perturbations propagate through faulted reservoirs.[1–5,12,16,17] However, these interpretations still largely focus on faults as the primary mechanically active structures, while reservoir-bounding stratigraphic interfaces are often treated as background geological boundaries rather than potential participants in the coupled hydraulic and mechanical response.

The hydraulic and mechanical perturbations generated by injection also have an important temporal dimension. Injection-induced loading should therefore be evaluated as a stressing-history problem, rather than only as a response to peak pressure. The timing, rate and duration of Coulomb failure stress change can determine whether slip-promoting conditions develop mainly during injection, emerge after shut-in, or persist over an extended period. This view is consistent with the rate-and-state seismicity framework of Dieterich,[18] in which seismicity rate depends on stressing history, and with the extension of Heimisson and Segall[19] to arbitrary stressing histories. Field observations and hydro-mechanical models from wastewater-injection settings further show that seismicity can migrate and evolve with injection-rate history because pressure diffusion and stress redistribution continue during and after injection.[4,5,12,20] For layered reservoirs, these studies indicate that injection protocols should be assessed in terms of the full loading history, rather than by maximum pressure alone.

Reservoir-bounding stratigraphic contacts are not a single class of discontinuity. They include depositional contacts and bedding planes, erosional unconformities and their associated palaeo-weathering profiles, weathered or altered horizons, and tectonically overprinted or mineralized seams. These classes differ in both their hydraulic and their mechanical behaviour, and they are therefore not interchangeable as model elements. Bedding planes and depositional contacts are surfaces of mechanical weakness and commonly host clay-, organic- or mica-rich partings. Their normal stiffness and shear strength are controlled by asperity geometry, infill mineralogy and aperture, and they typically exhibit strongly non-linear, stress-dependent closure and dilatancy.[21,22] Erosional unconformities may be associated with weathered, leached or karstified horizons and with coarse lag deposits. They can therefore act either as laterally extensive high-transmissivity pathways or, where weathering residues and diagenetic cements dominate, as baffles or local seals. Palaeo-weathering profiles preserved beneath unconformities are commonly characterized by reduced elastic moduli, elevated porosity and a permeability that decays with depth into the parent rock. Where such surfaces have been tectonically reactivated, they may contain cataclastic or gouge material whose frictional strength and permeability differ markedly from those of the intact wall rock. Structural diagenesis further modifies these contacts after deposition, through cementation, dissolution and compaction that are themselves sensitive to the local stress and fluid state.[23] Consequently, a fracture-dominated bedding plane behaves as a stiff, stress-sensitive conduit, whereas a clay-rich weathering residue or a mineralized seam may behave as a compliant, low-permeability barrier, even where both separate the same pair of formations. In this study we represent this variability through a single effective, finite-thickness hydro-mechanical interface zone at each reservoir boundary, characterized by stiffness, permeability, storage and Biot coefficient (Section 2.4). The individual micro-scale mechanisms listed above are therefore not resolved; they motivate the parameter ranges considered here and the sensitivity analyses reported in Section 4.3.

Reservoir-bounding stratigraphic contacts deserve closer attention because they commonly coincide with hydraulic and mechanical contrasts in layered reservoirs. Reservoir–caprock and reservoir–basement interfaces may differ from adjacent units in stiffness, permeability, storage capacity, and effective stress conditions, thereby influencing the evolution of pressure and stress perturbations within faulted layered reservoirs. Studies of caprock integrity have shown that resistance to hydraulic fracturing and sealing performance depend on coupled hydraulic-mechanical processes and site-specific layer properties.[6,7] Similarly, clay-rich interbeds can deform differently from adjacent formations during injection, and mechanical stratification can influence injection-induced seismic moment release in layered rocks.[8,9] These studies demonstrate the importance of stratigraphic architecture, but they have not fully resolved how thin reservoir-bounding interfaces affect Coulomb loading within a coupled reservoir-interface-fault system. This gap is important because such contacts are commonly characterized in terms of lithology, sealing capacity, or permeability contrast, whereas their role as mechanically responsive elements within faulted layered reservoirs remains insufficiently quantified.

Evidence from natural discontinuities and in situ injection experiments further supports the need to consider reservoir-bounding interfaces as potentially responsive hydro-mechanical elements. In situ injection experiments have shown that fluid injection can trigger aseismic slip on natural discontinuities, with associated stress transfer potentially contributing to microseismic activity.[10,24] Hydromechanical modeling has further shown that permeability enhancement along slipping faults can modify pressure diffusion, stress perturbations, and the development of injection-induced aseismic slip.[10,25] However, these studies mainly concern faults or natural discontinuities rather than reservoir-bounding stratigraphic contacts. For layered reservoirs, this raises the question of whether reservoir-bounding interfaces may undergo transmissivity changes associated with possible slip, dilation, damage, or hydraulic opening, and how such changes would affect the coupled hydraulic and mechanical response. This issue is particularly important where stratigraphic contacts intersect faults, yet a unified assessment of how interface properties, injection-rate history, and possible interface transmissivity evolution jointly influence injection-induced Coulomb loading remains limited. Addressing this gap requires a framework that explicitly represents reservoir-bounding interfaces as distinct hydro-mechanical components while tracking the time-dependent evolution of Coulomb loading during and after injection.

This study asks how stratigraphic interfaces and injection history control the pressure and stress pathways that generate Coulomb loading on reservoir-bounding contacts and on faults in layered reservoirs. We address this question with a coupled Biot poroelastic model of a representative caprock–reservoir–basement system in which the reservoir–caprock and reservoir–basement contacts are explicitly resolved as mechanically and hydraulically distinct zones. Rather than forecasting earthquake magnitude or simulating spontaneous dynamic rupture, the study evaluates how interface properties, injection duration and interface transmissivity evolution shape the time-dependent and spatial distribution of Coulomb loading. This study makes three contributions. Stratigraphic interfaces are represented as explicit finite-thickness hydro-mechanical zones, rather than as property jumps. Injection history is treated as a stressing-history problem at fixed injected mass. The intersection between a stratigraphic contact and a fault is identified as a locus at which loading can be focused without a corresponding rise in well pressure. This focus is consistent with recent efforts to connect physics-based modeling with geological characterization and operational assessment for induced-seismicity risk management in geo-energy systems.[12,26]

Methodology

This section describes the poroelastic loading framework, the post-processing workflow used to compute Coulomb loading and relative seismicity-rate indicators, and the reservoir-scale model configuration. The coupled evolution of pore pressure and solid-skeleton deformation in saturated porous media is described using the classical Biot poroelastic formulation. The resulting pressure and stress histories are then projected onto stratigraphic interfaces and a reservoir-crossing fault to evaluate Coulomb failure stress change and a Dieterich-type relative seismicity-rate indicator. These quantities are interpreted as diagnostic indicators of time-dependent loading tendency, rather than as simulations of spontaneous slip, rupture propagation, or earthquake

magnitude. The poroelastic implementation is verified against Mandel's problem, and the reservoir-scale model is then defined by its geometry, material properties, boundary conditions, injection protocols, and prescribed interface transmissivity evolution. The study is a deterministic, physics-based numerical experiment. No sampling or hypothesis testing is involved; the reported quantities are model outputs rather than statistical estimates, and model uncertainty is examined through the sensitivity analyses presented in Sections 4.2 and 4.3.

Coupled Biot poroelastic formulation

We adopt the classical Biot poroelastic formulation to describe the transient coupling between pore-pressure diffusion and deformation of the solid skeleton during subsurface fluid injection. This formulation couples Darcy flow in the pore space with linear elastic deformation of the porous skeleton and provides the pressure and stress histories needed to evaluate Coulomb loading on faults and stratigraphic interfaces. It has been widely used to analyze injection-induced pore-pressure changes and poroelastic stress transfer in saturated porous media.[11,27–32] The formulation is used here under the following assumptions. (1) small deformation and linear elasticity of the solid skeleton; (2) full saturation, with pore-fluid and skeleton compressibility represented through a constrained specific storage coefficient; (3) isothermal conditions; (4) laminar flow governed by Darcy's law; and (5) piecewise homogeneous and isotropic properties within each geological unit and finite-thickness interface zone, with mechanical and hydraulic contrasts across stratigraphic boundaries.

The strain-displacement relation and the linear-elastic constitutive relation of the solid skeleton close the system, and mechanical equilibrium of the solid skeleton is governed by the quasi-static momentum balance equation,

$$\nabla\cdot\boldsymbol{\sigma} = \boldsymbol{0},\ \boldsymbol{\sigma}^{e} = 2G\boldsymbol{\varepsilon} + \lambda(\mathrm{tr}\boldsymbol{\varepsilon})\mathbf{I},\ \ \text{and}\boldsymbol{\varepsilon} = \frac{(\nabla\mathbf{u} + \nabla\mathbf{u}^{T})}{2}, \tag{1}$$

where $\boldsymbol{\sigma}$ is the total stress tensor, $\mathbf{u}$ is the solid-skeleton displacement, $\boldsymbol{\varepsilon}$ is the small-strain tensor and $\boldsymbol{\sigma}^{e}$ is the effective stress tensor of the solid skeleton. G and λ are the drained Lamé parameters, related to the drained Young's modulus E and Poisson's ratio ν by $G = E\,/\,[2(1+\nu)]$ and $\lambda = E\nu\,/\,[(1+\nu)(1-2\nu)]$. Eqs. (1)–(4) form a complete system for the dependent variables $\mathbf{u}$ and p. Sign conventions are stated once here for this study. Stress components are positive in tension, pore pressure is positive in compression, and a compressive normal traction therefore corresponds to a negative value of the corresponding normal stress component. Because the analysis focuses on perturbations relative to an initially self-equilibrated state, gravitational body forces are neglected. The total stress is related to effective stress and pore pressure through the Biot effective stress principle,

$$\boldsymbol{\sigma} = \boldsymbol{\sigma}^{e} - \alpha p\mathbf{I}, \tag{2}$$

where α is the Biot-Willis coefficient, p is pore pressure, and $\mathbf{I}$ is the identity tensor. Fluid mass conservation is expressed as

$$\alpha\nabla\cdot\mathbf{v}^{s} + \nabla\cdot\mathbf{w} - S_{\varepsilon}\frac{\partial p}{\partial t} = q, \tag{3}$$

where $\mathbf{v}^{s}$ is the solid-skeleton velocity, $\mathbf{w}$ is the Darcy flux of the pore fluid relative to the solid skeleton, S_{ε} is the constrained specific storage coefficient, and q is the prescribed fluid source term. The first term represents pore-volume changes induced by skeleton deformation, the second term represents the divergence of relative fluid flux, and the third term represents fluid-volume change associated with pore-pressure variation.[31] The relative fluid flux follows Darcy's law,

$$\mathbf{w} = -\frac{\kappa}{\mu}\nabla p, \tag{4}$$

where κ is the intrinsic permeability tensor and μ is the dynamic viscosity of the pore fluid, taken as $\mu = 1.0\times10^{-3}$ Pa · s. The gravity term in Darcy flow is neglected, consistent with the perturbation-based treatment of stress and pressure changes. Spatial variations in permeability, storage, stiffness, and Biot-Willis coefficient among the reservoir, caprock, basement, and interface layers control the coupled pressure diffusion and poroelastic stress transfer.

Coulomb loading and relative seismicity-rate indicator

Injection-induced stress and pore-pressure perturbations can promote slip tendency on pre-existing discontinuities, including faults and stratigraphic interfaces. To distinguish the structural origin of the modeled response, we use the terms primary seismicity and secondary seismicity throughout this study. Primary seismicity denotes the relative seismicity-rate response associated with Coulomb loading on the reservoir-crossing fault, whereas secondary seismicity denotes the corresponding response along stratigraphic interfaces, including the reservoir–caprock and reservoir–basement interfaces. In this framework, these terms refer to diagnostic loading and rate responses on different geological structures, not to direct simulations of spontaneous slip, rupture propagation, or earthquake occurrence. Slip tendency is quantified using the Coulomb failure stress change ΔCFS, which incorporates the combined effects of shear stress change, normal stress change and pore-pressure change. Two quantities are distinguished throughout this study. ΔCFS is retained as a slip-tendency index that is directly comparable with the induced-seismicity literature. The rate-and-state model is instead forced by ΔS, which follows Heimisson and Segall[19] and is defined in the next section. Given the distinct mechanical and hydraulic properties of the reservoir–caprock and reservoir–basement interfaces, interface-specific Coulomb failure stress changes are evaluated as follows,

$$\Delta\mathrm{CFS} = \Delta\tau_{s} - f\cdot\Delta\sigma_{n} + f\cdot\Delta p, \tag{5}$$

where f is the friction coefficient. Laboratory measurements indicate that rock and mineral friction coefficients span a broad range, commonly from weak phyllosilicate-rich materials to stronger quartz- or feldspar-rich surfaces.[33] We prescribe $f = 0.5$ as a reference value to compare relative loading patterns among interfaces, faults, and injection protocols. This value should therefore be interpreted as a screening parameter rather than a calibrated strength for a specific caprock or basement interface. Sensitivity to f can be evaluated in future site-specific applications where mineralogy, roughness, clay content, and pore-fluid conditions are constrained.

The sign conventions are stated here explicitly. $\Delta\tau_{s}$ is the change in the shear traction resolved on the discontinuity, taken positive in the assumed slip direction. $\Delta\sigma_{n}$ is the change in total normal traction across the discontinuity, taken positive in compression, and Δp is the change in pore pressure. The assumed slip direction is the direction of injection-induced lateral expansion of the reservoir, that is, the $+x$ direction in the model section. With this convention $\Delta\tau_{s} > 0$ indicates shear loading that promotes slip on the discontinuity in the direction of the assumed sense of movement, and a positive ΔCFS indicates an increase in slip tendency. The sign of $\Delta\tau_{s}$ is set by the sense in which the adjacent units accommodate the lateral expansion of the pressurized reservoir. Above the reservoir, the relatively stiff caprock resists expansion. The shear traction transmitted across the reservoir–caprock contact therefore changes in the opposite sense to the shear traction that develops within the reservoir. This appears as a sign reversal of $\Delta\tau_{s}$ relative to the injection-induced shear in the reservoir. Below the reservoir, the still stiffer basement accommodates and transmits the shear deformation more coherently over a larger distance. $\Delta\tau_{s}$ on the reservoir–basement contact therefore has the same sign as the corresponding quantity above the reservoir, and a broader spatial footprint. The asymmetry between the two contacts therefore reflects the combined effect of the stiffness contrast and of the differing top and bottom boundary conditions. The

two contributions are separated by the control simulations reported in Section 4.2.

The full stress tensor is resolved onto each surface rather than assuming a single shear component. For a planar surface with unit normal $\mathbf{n} = (-\sin\delta, 0, \cos\delta)$ in the x–z section, where δ is the dip measured from the horizontal. The traction vector is $\mathbf{t} = \boldsymbol{\sigma} \cdot \mathbf{n}$ and the normal traction is $\sigma_n = \mathbf{t} \cdot \mathbf{n}$. The signed shear stress change is $\Delta\tau_s = \Delta(\mathbf{t} \cdot \hat{\mathbf{s}})$, with $\hat{\mathbf{s}}$ the unit vector in the assumed slip direction within the plane. For the horizontal interfaces ($\delta = 0$) this reduces to $\Delta\tau_s = \Delta\sigma_{xz}$, which is why the interface results are unaffected by the tensor resolution. For the dipping fault ($\delta = 60°$) it does not, and all fault quantities are computed from the resolved traction. The resolution has been verified against closed-form solutions for two different stress states over dips of 0–90° (Section 2.3).

To represent the time-dependent seismicity response to stress perturbations, we employ the rate-and-state friction formulation of Dieterich.[18] The evolution of the seismicity rate relative to the background level is governed by

$$\frac{dR}{dt} = \frac{R}{t_a}\left(\frac{\dot{\tau}}{\dot{\tau}_0} - R\right), \tag{6}$$

where R is the seismicity rate normalized to the background rate, t_a is the characteristic relaxation time, $\dot{\tau} = \partial\Delta\tau / \partial t$ is the Coulomb stressing rate, and $\dot{\tau}_0$ is the reference background stressing rate (taken as 10^{-3} MPa / year). The relaxation time t_a is defined as $t_a = A\bar{\sigma}/\dot{\tau}_0$, where A is the dimensionless constitutive parameter and $\bar{\sigma}$ is the effective normal stress. We adopt $A = 0.005$ based on laboratory friction experiments and choose a representative $\bar{\sigma} = 10$ MPa for the modeled system, yielding $t_a = 50$ years for the prescribed $\dot{\tau}_0$. This formulation describes how a prescribed Coulomb stressing history would modify the relative rate indicator during injection and after shut-in. To isolate physically driven differences between structural elements, we use the same rate-and-state parameter set ($A\bar{\sigma}$, $\dot{\tau}_0$) for both interfaces and faults; therefore, contrasts in $R(t)$ arise solely from the simulated Coulomb stressing histories and stressing rates $\dot{\tau}(t)$, rather than from structure-specific parameter tuning.

For the forcing function we follow Heimisson and Segall,[19] who show that the quantity entering the rate-and-state formulation is not the conventional Coulomb stress but

$$\Delta S = \Delta\tau_s - \mu^*(\Delta\sigma_n - \Delta p), \text{ with } \mu^* = \tau_0 / \sigma_0', \tag{7}$$

where τ_0 and σ_0' are the background shear stress and the background effective normal stress on the plane. The conventional form $\Delta\tau - f\,\Delta\sigma$ is the special case $\mu^* = f$, corresponding to a plane at or near the friction limit. For a plane carrying no background resolved shear stress ($\tau_0 = 0$), such as a strictly horizontal contact in an Andersonian stress state, $\mu^* = 0$ and the rate response is driven by $\Delta\tau_s$ alone. The reference background stress state used to evaluate μ^* is defined in Section 2.5, and all rate results are reported as a function of μ^*.

The relative rate indicator $R(t)$ is evaluated element-wise on the modeled stratigraphic interfaces and fault following the Coulomb-stressing workflow of Chang and Segall.[11] From the coupled poroelastic simulations, we extract time series of shear stress change, normal stress change, and pore-pressure change. These quantities are combined to compute $\Delta S(t)$, from which the stressing rate is obtained using cubic-spline differentiation. The Dieterich-type ordinary differential equation is then solved for the normalized relative rate indicator $R(t)$, initialized at $R(0) = 1$. Time integration is performed with an adaptive embedded Runge-Kutta scheme (Tsitouras 5/4),[34] using relative and absolute tolerances of 10^{-6} and 10^{-10}, respectively, to maintain accuracy over the full simulation interval and during rapid stress change transients.

The Dieterich formulation is used here as a one-way mapping from Coulomb stressing history to a normalized relative rate response. The poroelastic model first provides $\Delta S(t)$ and its time derivative, and these histories are then used to compute $R(t)$. The computed $R(t)$ does not feed back into the mechanical calculation; therefore, the model does not represent slip-induced stress redistribution, dynamic rupture, earthquake interactions, or permeability changes caused by actual slip. This treatment is appropriate for comparing how different injection histories and interface hydraulic states modify loading tendency, but it should not be interpreted as a complete earthquake-cycle or rupture model.

Verification against Mandel's problem

The classical Mandel's problem is employed to verify the fully coupled poroelastic formulation. In this benchmark, a saturated poroelastic slab with width $2b$ and height $2a$ is instantaneously compressed between two rigid, impermeable, and frictionless plates under a uniform vertical force of $2F$ applied on the top and bottom surfaces. The lateral boundaries are traction-free ($\sigma_{xx} = 0$) and fully drained ($p = 0$). Because of plane-strain conditions and double symmetry, only the quarter-domain ($0 \le x \le b$, $0 \le z \le a$) is modeled, with appropriate symmetry boundary conditions, as illustrated in Fig. 1a. The numerical simulation utilizes a structured quadrilateral finite element mesh (Fig. 1b). The analytical solution for pore pressure evolution and distribution is provided by Ferronato *et al.*,[35]

The boundary conditions are stated completely here. On the two loading platens the plate is frictionless, so the shear traction vanishes ($\sigma_{xz} = 0$) while the vertical displacement is prescribed. On the symmetry planes of the reduced quarter domain ($x = 0$ and $z = 0$) the normal displacement and the shear traction both vanish. On the drained lateral boundary ($x = b$) the traction-free condition implies $\sigma_{xx} = 0$ and $\sigma_{xz} = 0$ in addition to $p = 0$. The Mandel benchmark verifies the coupled pressure diffusion and volumetric poroelastic response, the Mandel–Cryer pressure evolution, reproduced here within the reported tolerance. It does not by itself exercise the boundary conditions that give rise to a shear traction, because the shear traction vanishes on all of its boundaries. An independent verification of the shear and deviatoric response is therefore included here. The computed total stress field is compared with the analytical Mandel stress solution ($\sigma_{zz} = -P$ constant, with $\sigma_{xx}(x, t)$ following from the analytical pressure field through the constitutive relations). Two simple-shear patch tests are compared with the closed-form elasticity solution, one on a homogeneous block and one on a three-layer stack with the caprock, reservoir and basement moduli used in this study. The exact solution has a uniform shear traction $\sigma_{xz} = \tau$, identically zero pore pressure and a displacement gradient τ/G_i in each layer, so that the layered test also verifies the transmission of a shear traction across a stiffness contrast. The computed shear stress matches the closed-form values in both patch tests (homogeneous, 7.576 MPa against 7.600 MPa; layered, 12.936 MPa against 12.970 MPa), while the transverse stress components average below

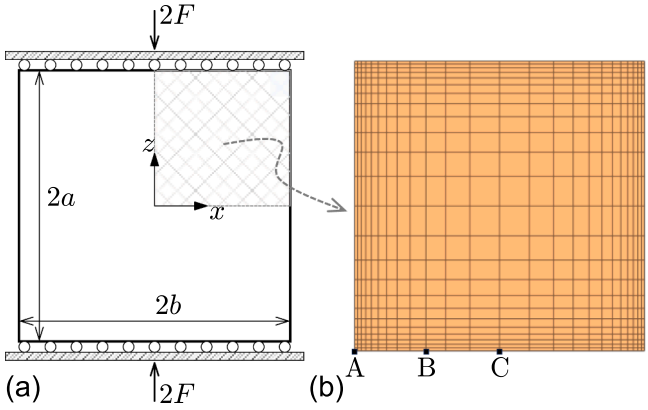


Fig. 1. Setup for Mandel's problem in the verification of the poroelastic formulation. (a) Geometry, loading, and boundary conditions (shaded region indicates the computational quarter-domain). (b) Structured quadrilateral finite element mesh used in the simulation (points A, B, and C are selected for comparison).

0.032 MPa, as the exact solution requires. The resolution of the stress tensor onto planes of arbitrary dip is verified separately. For the two stress states of these models the resolved shear traction matches the closed forms $|\tau| = (P/2)\sin 2\delta$ (Mandel) and $|\tau| = \tau_0 |\cos 2\delta|$ (simple shear) over dips of 0–90°.

$$p\left(x,t\right) = 2p_0 \sum_{n=1}^{\infty} \frac{\sin \alpha_n}{\alpha_n - \sin \alpha_n \cos \alpha_n}\left(\cos \frac{\alpha_n x}{a} - \cos \alpha_n\right)\exp\left(\frac{-\alpha_n^2 ct}{a^2}\right), \tag{8}$$

where the coefficients α_n are the positive roots of the characteristic equation

$$\tan \alpha_n = \frac{1-\nu}{\nu_u - \nu}\alpha_n, \tag{9}$$

with the undrained Poisson's ratio ν_u defined as

$$\nu_u = \frac{\nu E S_\varepsilon + \alpha^2(1-2\nu)(1+\nu)}{E S_\varepsilon + 2\alpha^2(1-2\nu)(1+\nu)}. \tag{10}$$

The consolidation coefficient is expressed as

$$c = \frac{\kappa E(1-\nu)}{\mu E(1-\nu)S_\varepsilon + \mu\alpha^2(1+\nu)(1-2\nu)}. \tag{11}$$

The material parameters for the verification, adopted from Guo *et al.*,[36] are listed in Table 1. For simplicity, a square slab geometry with $a = b = 1$ m is used, along with an applied force $F = 100$ N (corresponding to a slab thickness of 0.01 m). To approximate instantaneous loading in the numerical model, the force F is applied incrementally over a short loading period of 10 s, divided into 200 time steps with a constant time increment of 0.05 s. The numerical results for the pore pressure field are compared against the analytical solution. The comparison demonstrates that the model accurately captures the Mandel–Cryer effect, in which the pore pressure in the central region initially increases above its starting value before dissipating. As shown in Fig. 2a, the normalized pore pressure profiles along the normalized horizontal distance at various normalized times exhibit excellent agreement between numerical and analytical results across the domain. Similarly, Fig. 2b highlights the temporal evolution of normalized pore pressure at selected points (A, B, and C), confirming the model's fidelity in capturing the initial pressure buildup and subsequent decay associated with the Mandel–Cryer effect. This close match validates the accuracy of the implemented poroelastic formulation in capturing transient coupled hydro-mechanical behavior. Furthermore, Fig. 3 depicts the spatial distribution of pore pressure immediately after loading, showing a nonuniform pressure field with higher values concentrated in the central region, consistent with the expected poroelastic response under constrained drainage conditions.

Reservoir-scale model configuration

The reservoir-scale model is designed to examine how stratigraphic architecture and injection history affect pressure diffusion, poroelastic stress transfer, and Coulomb loading in a layered reservoir system. A representative caprock–reservoir–basement configuration is used to compare loading patterns under controlled stratigraphic and operational conditions. The geometric configuration, boundary conditions, and mesh are shown in Fig. 4. The model domain represents a 15 km × 2.7 km vertical cross-section through three geological units. A 0.6 km thick caprock layer characterized by low permeability to act as a sealing barrier, a 0.1 km thick permeable reservoir layer serving as the primary injection target, and a 2.0 km thick basement layer representing the underlying crystalline or sedimentary foundation with intermediate hydraulic properties. To represent the transitional hydro-mechanical behavior at stratigraphic interfaces, where stiffness and permeability contrasts may promote localized loading, thin interface layers are explicitly incorporated at both the reservoir–caprock and reservoir–basement boundaries. These interface zones are assigned average material properties to reflect gradual transitions in stiffness, permeability, and poroelastic parameters between adjacent formations. The 5 m interface thickness is an effective model thickness used to resolve the hydro-mechanical transition zones within the finite-element mesh and should not be interpreted as a universal physical thickness of natural stratigraphic contacts. In field applications, this effective interface thickness and material properties of the reservoir, caprock, basement, interface zones, and fault zone should be constrained by site-specific data. Interface continuity and thickness may be inferred from core descriptions, borehole image logs, and seismic attributes; stiffness contrasts from laboratory tests and geophysical logging; permeability and storage parameters from hydraulic tests and pressure-transient analysis; and fault-interface geometry from structural interpretation and microseismic monitoring. The present model is therefore intended as a process-based screening tool rather than a site-calibrated hazard forecast.

The interface zones are assigned a thickness of 5 m. This value is an effective model thickness, representing the length scale over which the properties of a transitional contact are distributed, and it is not a universal physical thickness. The sensitivity of the results to it is quantified in Section 4.3 by repeating the reference simulation with 1 m, 20 m and 50 m interface zones and with the interface zones removed altogether. The reservoir-crossing fault is resolved as an explicit body 20 m wide in horizontal section with a dip of 60°, corresponding to a true thickness of 17.3 m. It is assigned the homogeneous equivalent properties listed in Table 2; its position, dip and thickness are reported in Fig. 4. Two fault geometries are used in this study. In the conductive configurations of Sections 3.2 and 3.3 the fault is a reservoir-crossing body that extends from the base of the basement to the free surface. In the sealing and isolated-fault configuration of Section 3.1, and of the control and sensitivity experiments of Sections 4.2 and 4.3, it is resolved only within the basement and terminates 200 m below the reservoir–basement contact, so that it remains geometrically isolated from the reservoir. The fault permeability differs between the two configurations. The conductive fault uses the value given in Table 2, whereas in the sealing and isolated-fault configuration the fault is assigned 1.0×10^{-21} m^2, four orders of magnitude below the surrounding basement, so that it acts as a hydraulic barrier rather than a conduit.Fig. 4

Boundary conditions are prescribed to represent a simplified reservoir-scale injection setting while maintaining numerical stability. The top boundary is treated as a free surface with fully drained conditions ($p = 0$), permitting unrestricted vertical displacement and fluid drainage to simulate atmospheric exposure. The bottom boundary is assigned a roller mechanical condition and an impermeable hydraulic condition to represent a no-flow lower boundary. The left boundary is constrained by roller conditions, with fluid injection modeled as a constant mass flux applied uniformly along the reservoir depth at this boundary (line injection). The right lateral boundary is constrained by roller conditions with a fixed pore pressure ($p = 0$) to mimic far-field hydrostatic equilibrium and lateral drainage. This configuration allows asymmetric pressure diffusion from the injection boundary to be analyzed. The shear tractions vanish on all external boundaries of the model as well as on its symmetry planes, the free surface, the roller

Table 1
Material parameters for Mandel's problem.

Parameters	Values
Young's modulus, E (GPa)	0.1
Poisson's ratio, ν	0.25
Porosity, ϕ	0.375
Permeability, κ (m^2)	1.02×10^{-12}
Fluid viscosity, μ (Pa·s)	1.0×10^{-3}
Biot-Willis coefficient, α	1.0
Constrained specific storage, S_ε (Pa^{-1})	1.65×10^{-10}

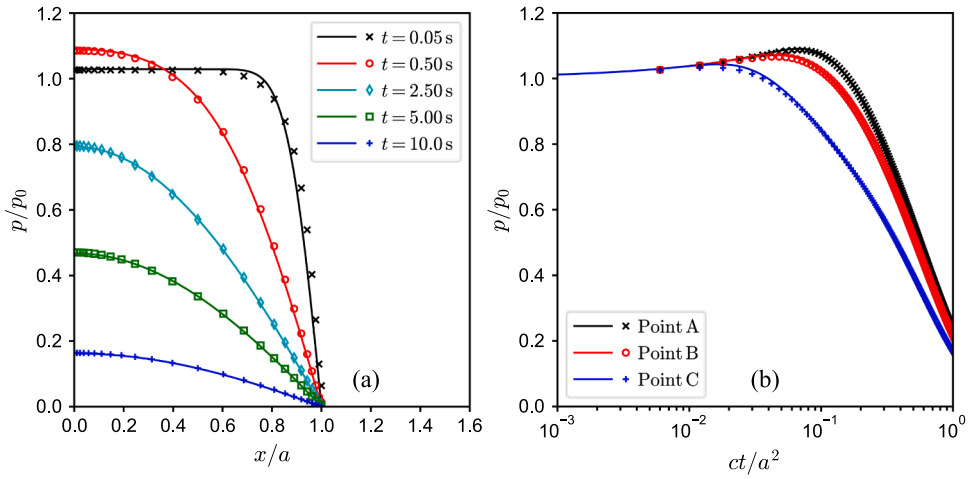


Fig. 2. Comparison between analytical and numerical results for Mandel's problem, with (a) normalized pore pressure (p / p_0) against normalized horizontal distance (x / a) at five times, given in seconds (ct / a^2 = 0.006, 0.06, 0.30, 0.60 and 1.20); (b) normalized pore pressure against normalized time (ct / a^2) at points A (x / a = 0), B (x / a = 0.246) and C (x / a = 0.50). In both panels the solid lines are the analytical solution of Section 2.3 and the open markers are the finite-element results; a colour denotes one time in (a) and one point in (b). The numerical series follow the analytical solution at every time, including the Mandel–Cryer overshoot of the central pressure.

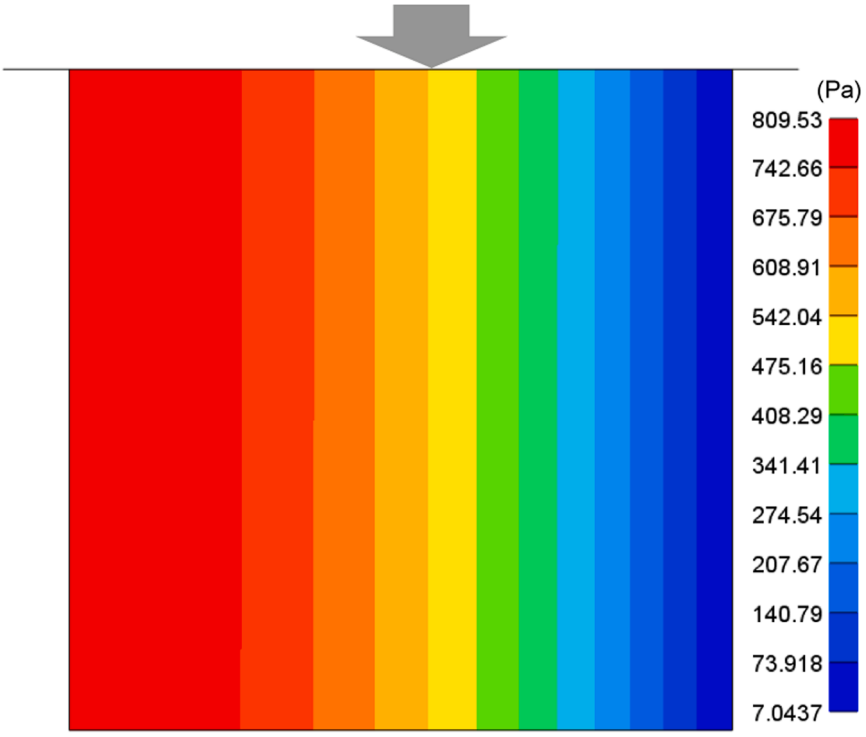


Fig. 3. Simulated pore pressure (p) distribution immediately after loading in Mandel's problem.

boundaries and the injection plane. The interface and fault shear loading reported in this study therefore arises entirely from internal poroelastic gradients, rather than from an applied boundary shear.

To ensure that the drained far-field boundary could influence the inferred persistence and spatial extent of pressure and stress changes, we follow the scale-analysis approach of Chang and Segall[11] and evaluate the characteristic hydraulic diffusion length $l_d = \sqrt{ct}$, where $c = \kappa / (\mu S_\varepsilon)$ is computed from the permeability, viscosity, and storage parameters listed in Table 2. Over the 300-day analysis period, l_d remains small relative to the lateral model extent, indicating limited interaction between the pressure front and the far-field boundary. Consistent with this scale separation and with the boundary-condition sensitivity considerations discussed by Chang and Segall,[11] additional tests with an enlarged lateral extent (or, alternatively, a no-flow far-field boundary) produce only minor changes in the key response metrics (peak Δp, peak $\Delta\tau$, and the duration of elevated seismicity rate). We therefore interpret the protocol-dependent responses as controlled primarily by poroelastic diffusion and coupling within the layered system rather than by far-field boundary drainage.

Initial conditions assume a stress-free and pressure-equilibrated state prior to injection, with perturbations in stresses $\boldsymbol{\sigma}(\mathbf{x}, t = 0) = 0$ and pore pressure $p(\mathbf{x}, t = 0) = 0$, focusing the analysis on injection-induced changes.[11] The model is initialized at a pre-injection equilibrium state and analyzed in terms of perturbations; thus, neglecting gravity and

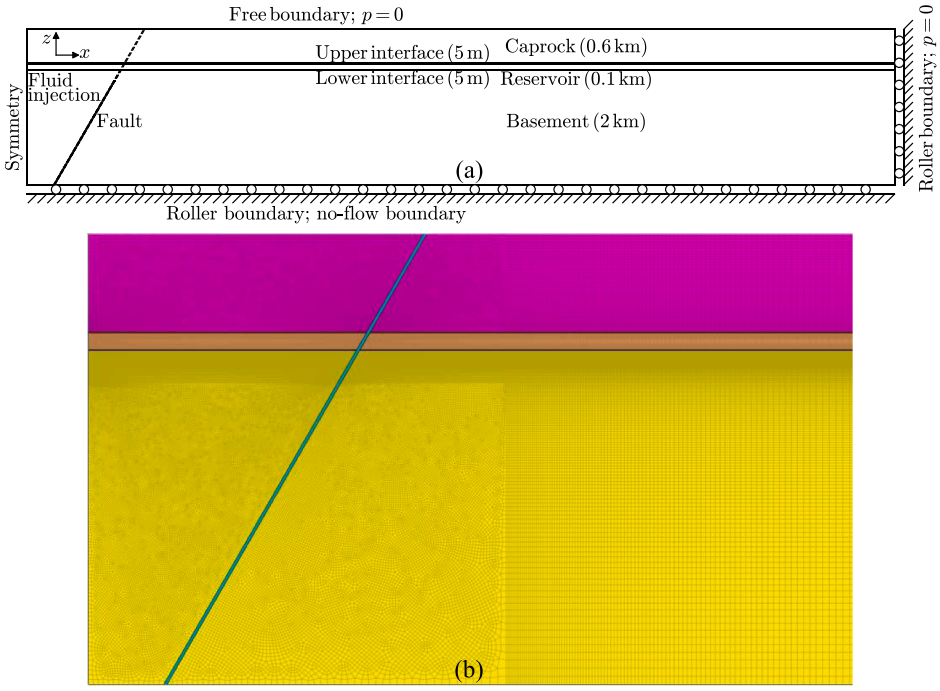


Fig. 4. Plane-strain model setup for reservoir injection, implemented as a thin three-dimensional finite-element slab of 15 km × 2.7 km. (a) Schematic of the geometry, stratigraphic units and boundary and loading conditions, labelled with the unit thicknesses (caprock 600 m, reservoir 100 m, basement 2000 m) and the interface thickness (5 m), and showing the reservoir-crossing fault, 20 m wide at a 60° dip (17.3 m true thickness); the injection boundary is at x = 0. (b) The computational mesh, coloured by stratigraphic unit, showing the caprock, the two interface layers, the reservoir, the basement and the reservoir-crossing fault. The model contains 166,051 hexahedral (8-node) elements and 333,314 nodes, with local refinement across the interface layers, within the fault zone and along the injection boundary.

Table 2
Material parameters for reservoir simulation during fluid injection.

Parameters	Caprock	Reservoir	Basement	Upper interface	Lower interface	Fault
Young's modulus, E (GPa)	29.9	17.48	60	23.69	38.74	14.4
Poisson's ratio, ν	0.3	0.15	0.2	0.225	0.175	0.2
Density, ρ (kg/m^3)	2600	2500	2740	2550	2620	2500
Porosity, ϕ	0.1	0.25	0.05	0.175	0.15	0.02
Permeability, κ (m^2)	1.0×10^{-19}	6.4×10^{-14}	2.0×10^{-17}	8.0×10^{-17}	1.13×10^{-15}	1.0×10^{-13}
Biot-Willis coefficient, α	0.35	0.55	0.24	0.45	0.395	0.79
Constrained specific storage, S_ε (Pa^{-1})	1.26×10^{-11}	7.04×10^{-11}	6.64×10^{-12}	4.15×10^{-11}	3.85×10^{-11}	8.13×10^{-11}

Note: The caprock, reservoir, basement and fault values are from Chang and Segall.[11] The upper- and lower-interface values are effective properties of the transitional zones, obtained from the bounding units by arithmetic averaging for E, ν, ρ, ϕ, α and S_ε and geometric averaging for permeability.

using $p = 0$ and $\boldsymbol{\sigma} = 0$ at $t = 0$ does not influence protocol-dependent trends in Δp and $\Delta\tau$. Background stresses mainly affect absolute failure proximity (e.g., through $\bar{\sigma}$ in the rate-and-state formulation) rather than the relative differences among injection protocols. Spatial discretization uses a thin-slab three-dimensional domain meshed with an unstructured hexahedral finite-element grid (Fig. 4b). The simulations are mechanically interpreted as two-dimensional plane-strain models in the x–z section. They are implemented using a thin three-dimensional finite-element slab only for compatibility with the numerical implementation. Out-of-plane displacements are constrained on the front and back faces, and only one element is used across the slab thickness; therefore, field variables are effectively invariant in the out-of-plane direction. All results reported below correspond to the x–z section. The mesh is locally refined near stratigraphic interfaces, faults, and the injection boundary to resolve steep gradients in pore pressure, displacement, and stress with manageable computational cost. Material properties for each stratigraphic unit, the interfaces, and the fault are summarized in Table 2, with selected parameters adopted from Chang and Segall.[11]

The coupled system is solved by a finite-element method that uses a monolithic Biot poroelastic formulation, a direct sparse solver and Newton-Raphson equilibrium iterations with adaptive time stepping (an automatic step-size controller with step cutback on failed convergence). The unstructured hexahedral mesh contains 166,051 solid elements and 333,314 nodes, with local refinement across the thin interface zones, within the fault zone and along the injection boundary. The friction coefficient f, the stress-transfer coefficient μ^*, the constitutive parameter A, the reference effective normal stress, the background stressing rate, the relaxation time, the ODE tolerances and the reference background stress state are given in Sections 2.2, 2.3 and 2.5.

The interface properties are effective values for a transitional contact, obtained from the bounding units, as arithmetic mean for E, ν, ρ, ϕ, α and S_ε, geometric mean for k (for example the upper-interface permeability is $\sqrt{(1.0 \times 10^{-19} \times 6.4 \times 10^{-14})} = 8.0 \times 10^{-17}$ m^2). The caprock, reservoir, basement and fault properties are from Chang and Segall.[11] For the geometry, the interface zones are 5 m thick, and the reservoir-crossing fault is an explicit body 20 m wide in horizontal section with a 60° dip, i.e., a true thickness of 17.3 m.

Two sets of simulations are designed to assess how operational history and interface hydraulic state influence Coulomb loading and

relative rate responses along the reservoir–caprock interface, reservoir–basement interface, and reservoir-crossing fault. First, the effects of injection duration and rate are explored by means of three distinct temporal profiles (illustrated in Fig. 5a). Short-duration (10 days at a high rate), medium-duration (30 days at a moderate rate), and long-duration (90 days at a low rate). All protocols inject the same total fluid mass, thereby isolating the role of rate history and duration while maintaining comparability in total injected mass. The loading history is divided into an injection phase followed by a post-injection (shut-in) phase, with injection terminating at day 10, 30, and 90 for the three protocols. The simulations of Section 3 are run for a fixed total duration of 300 days, measured from injection onset. Because the shut-in time differs among protocols, the available post-shut-in observation window is 290, 270, and 210 days for the 10-, 30-, and 90-day injections, respectively; therefore, we evaluate responses both at fixed absolute times (from injection onset) and at fixed times relative to shut-in (from the shut-in time) to ensure consistent cross-protocol comparison of peak, persistence, and migration characteristics. This allows evaluation of how injection timing control influences pressure buildup, stress diffusion, and poroelastic coupling. To ensure numerical accuracy and stability, adaptive dynamic time steps ranging from 1 s to 1 day are employed at all critical moments (e.g., the start and end of injection) during the loading process, with 1-day steps used at other times.

Second, we prescribe an end-member interface-transmissivity-growth scenario to examine the sensitivity of pressure and stress evolution to rapid hydraulic deterioration of an interface zone. The transmissivity increase is imposed 5 days after injection onset and implemented as a stepwise permeability increase within the injection-side segments of the interface zones (Fig. 5b), with the interface thickness held fixed. This timing and magnitude are prescribed rather than solved from a slip, damage, or hydraulic-fracturing criterion. The scenario therefore represents a controlled sensitivity test of interface hydraulic evolution, not a prediction of spontaneous interface breakdown or failure. The permeability change is imposed as a step at day 5 and is resolved over the 1-second adaptive time steps employed at this critical moment, avoiding numerical instability from an unresolved abrupt property change.

Background stress state and the stress-transfer coefficient μ^*

The forcing function of the rate model, Equation (7), requires the ratio of the background shear stress to the background effective normal stress on each plane, $\mu^* = \tau_0 / \sigma_0'$. We adopt a reference stress state appropriate to the modelled depth. A normal-faulting regime at about 2 km depth with a vertical effective stress $\sigma_v' = 30$ MPa and a horizontal effective stress $\sigma_h' = 10$ MPa, corresponding to a total-stress ratio of about 0.6 (an effective-stress ratio of 0.33). For a plane dipping by δ from the horizontal, the background tractions resolved on the plane are

$$\tau_0 = (\sigma_v' - \sigma_h') / 2 \sin 2\delta,\ \sigma_0' = (\sigma_v' + \sigma_h') / 2 - (\sigma_v' - \sigma_h') / 2 \cos 2\delta, \quad (12)$$

so that $\mu^* = 0$ for a perfectly horizontal plane ($\delta = 0$), but rises rapidly with small dip. For the reference state above, $\mu^* = 0.07$, 0.17, 0.32 and 0.44 for dips of 2°, 5°, 10° and 15° respectively, and approaches f for steeper dips (Fig. 6, Table 3). This is the quantitative basis for the position taken in this study. The limiting case of a strictly horizontal, Andersonian contact has no sensitivity to changes in effective normal stress, but real stratigraphic contacts are not perfectly horizontal planes. Bedding and contact surfaces carry depositional relief, regional dip and undulation, and on the flanks of structures and adjacent to faults their local dip is substantially larger than a few degrees. A dip of only a few degrees restores a substantial fraction of the sensitivity to $\Delta\sigma_n$ and Δp. The reservoir-crossing fault is assigned the μ^* corresponding to its own resolved orientation; for the 60° fault of this model Eq. (12) gives $\mu^* = 0.35$, since μ^* peaks at 0.58 for a 30° plane and falls again for steeper planes (Fig. 6a). All rate results are reported for $\mu^* = 0$, 0.1, 0.2, 0.3 and 0.5, with $\mu^* = 0.5$ retained as the conventional, critically stressed end-member. The interface results are additionally reported for $\mu^* = 0$, where the rate response is driven by $\Delta\tau_s$ alone. The sweep is carried out for all three injection protocols, so that the protocol dependence and the μ^* dependence of the rate response are separated (Fig. 6c, Table 3).

Results

We investigate the hydro-mechanical perturbations induced by fluid injection using coupled poroelastic simulations. The results are presented in terms of pore-pressure change Δp, resolved shear stress change $\Delta\tau_s$ or shear stress component $\Delta\sigma_{xz}$, Coulomb failure stress change $\Delta\tau$, and the relative seismicity-rate indicator $R(t)$. The emphasis is on how stratigraphic interfaces and injection protocols modify loading tendency, spatial footprint, and post-shut-in persistence, rather than on direct simulation of earthquake occurrence.

Secondary seismicity-rate response along stratigraphic interfaces

The secondary seismicity-rate response along stratigraphic interfaces in the sealing and isolated-fault configuration is governed by a coupled sequence in which injection protocol controls pore-pressure diffusion, which then drives poroelastic stress transfer. These fields combine to determine the Coulomb failure stress change ($\Delta\tau$) and ultimately the rate-and-state seismicity rate response $R(t)$. Even with identical total injected mass, changing the injection duration alters the timescale ratio between hydraulic loading and diffusion, thereby reshaping both the peak amplitude and the spatial and temporal footprint of positive Coulomb loading along the reservoir–caprock and reservoir–basement interfaces. The relative roles of the stiffness contrast and of the differing top and bottom boundary conditions in producing the asymmetry

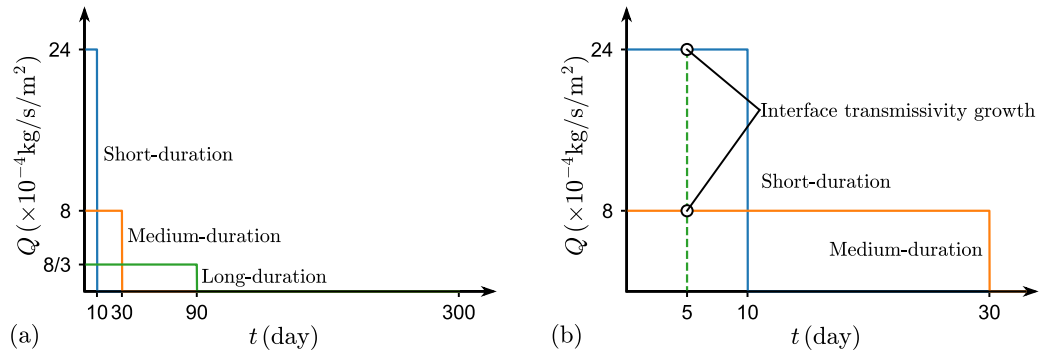


Fig. 5. Injection protocols and prescribed interface-transmissivity-growth scenario. (a) Constant mass injection rates prescribed for the short-, medium-, and long-duration scenarios that deliver the same total injected mass. (b) Timing of the prescribed interface-transmissivity-growth scenario, represented by a stepwise permeability increase within the injection-side segments of the interface zones.

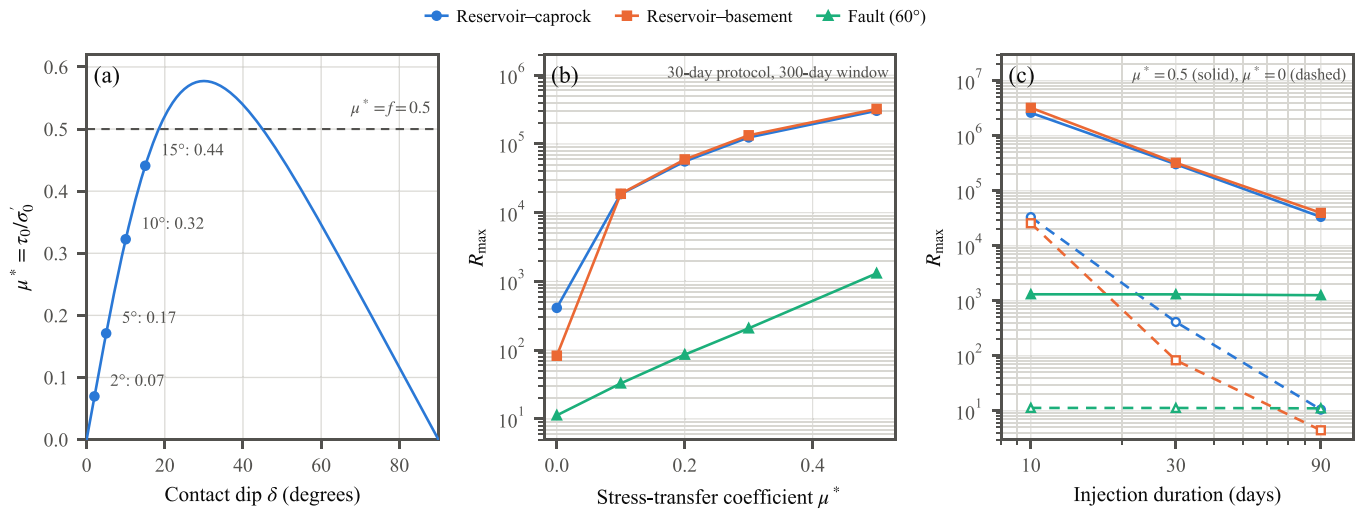


Fig. 6. Stress-transfer coefficient and the rate response. (a) $\mu^* = \tau_0/\sigma_0'$ as a function of the dip δ of a planar contact in the reference normal-faulting state ($\sigma_v' = 30$ MPa, $\sigma_h' = 10$ MPa); $\mu^* = 0$ for a strictly horizontal contact. (b) Peak relative rate R_{max} on the two interfaces and on the fault as a function of μ^* for the reference model (30-day protocol) over the full 300-day window. The ordering of the two contacts reverses between $\mu^* = 0$ and $\mu^* = 0.1$. At $\mu^* = 0$ the reservoir–caprock contact carries the larger response (412 against 83), while for $\mu^* \geq 0.1$ the reservoir–basement contact does. (c) R_{max} as a function of injection duration at $\mu^* = 0$ and $\mu^* = 0.5$. At fixed μ^* the interface response falls by roughly an order of magnitude for each step in injection duration, whereas the fault response is essentially protocol-independent.

Table 3
Sensitivity of the relative rate indicator to the stress-transfer coefficient μ^* for the reference model (30-day injection protocol, 300-day window). R_{max} is the maximum of $R(t)$ over the surface and over time and $t(R_{max})$ is the time at which it occurs; $\mu^* = 0.5$ is the conventional, critically stressed end-member. The interface peaks occur at or before shut-in, whereas the fault peak is reached at 99–168 days, so the fault values are evaluated over the full 300-day window.

Surface	Quantity	$\mu^* = 0$	0.1	0.2	0.3	0.5
Reservoir–caprock	R_{max}	412	1.9×10^4	5.6×10^4	1.2×10^5	3.0×10^5
Reservoir–basement	R_{max}	83	1.9×10^4	5.9×10^4	1.3×10^5	3.2×10^5
Fault (60°)	R_{max}	11.3	32.8	86	208	1.3×10^3
Reservoir–caprock	$t(R_{max})$ (d)	30	5	2	1	1
Reservoir–basement	$t(R_{max})$ (d)	13	4	2	1	1
Fault (60°)	$t(R_{max})$ (d)	157	168	161	142	99

between the two contacts are separated by the control simulations described in Section 4.2. Those experiments show that the stiffness contrast is not the controlling factor; the mechanical boundary conditions set the level of the response, while the residual asymmetry is associated with the hydraulic boundary asymmetry of the model.

At the end of the injection, the pore pressure fields already show strong protocol dependence (Fig. 7a-c). Short-duration, high-rate injection produces highly localized pressurization with steep along-interface gradients (Fig. 7a). This localization is expected because lateral hydraulic equilibration is limited by the short injection time and is further reinforced by the extremely low caprock permeability (1.0×10^{-19} m^2) and the sealing behavior of the isolated fault, which together suppress far-field pressure diffusion and favor near-field pressure buildup. In contrast, the medium-duration case distributes Δp more uniformly along both interfaces (Fig. 7b) because the 30-day injection phase allows appreciable lateral diffusion without producing the same near-field pressure spike. The long-duration, low-rate case further decreases the peak Δp (reported as approximately 10 MPa) while extending the pressure footprint (Fig. 7c), indicating that diffusion during injection mitigates sharp gradients but enlarges the region that experiences non-negligible pore pressure perturbation at shut-in.

At shut-in, the shear stress change along the interfaces (Fig. 7d-f) closely mirrors the Δp patterns (Fig. 7a-c), indicating that pressure-driven poroelastic deformation is the primary source of interface shear loading in the isolated-fault setting. Short-duration injection produces the most significant near-field shear stress perturbation, contributing appreciably to Coulomb loading on interfaces close to critical stress conditions. This amplification reflects the combined effect of localized overpressure and mechanical contrast across layers. In the model, the basement is substantially stiffer than the reservoir ($E = 60$ GPa vs. 17.48 GPa), which promotes stress concentration near stratigraphic interfaces and efficient transmission of deformation-induced shear stresses. A key insight from Fig. 7d-f is that the two interfaces do not scale identically. The reservoir–basement interface tends to exhibit a smaller local $\Delta\tau_s$ peak than the reservoir–caprock interface, yet its perturbations extend over a broader spatial range. This peak-footprint decoupling is not produced by the stiffness contrast. Removing that contrast in the control experiments leaves the lower-over-upper peak ratio unchanged (Section 4.2). It instead accompanies the hydraulic asymmetry of the model, and it means that moderate near-field loading can influence a larger portion of the lower interface.

Fig. 8 shows the shear loading in the x–z section at the end of the injection for each protocol. Every mesh node of the section is plotted at its horizontal position x, so that the shaded envelope at each x spans the variation of $\Delta\sigma_{xz}$ over depth. The envelope is widest in the immediate vicinity of the injection boundary and decays to near zero within the first few kilometres. Spatially, shear stress gradients are steepest near the injection boundary for the short-duration case and progressively flatten as injection duration increases, reflecting a shift from localized loading to diffusion-smoothed stress change. At a fixed injected mass, the peak magnitude of the envelope decreases as the injection duration lengthens. Because $R(t)$ depends on both stress amplitude and stressing rate, injection duration changes the relative rate response even when the injected mass is fixed. Short injection imposes a strong but brief near-field stressing-rate pulse, whereas long injection maintains smaller but more persistent stress changes over a larger region.

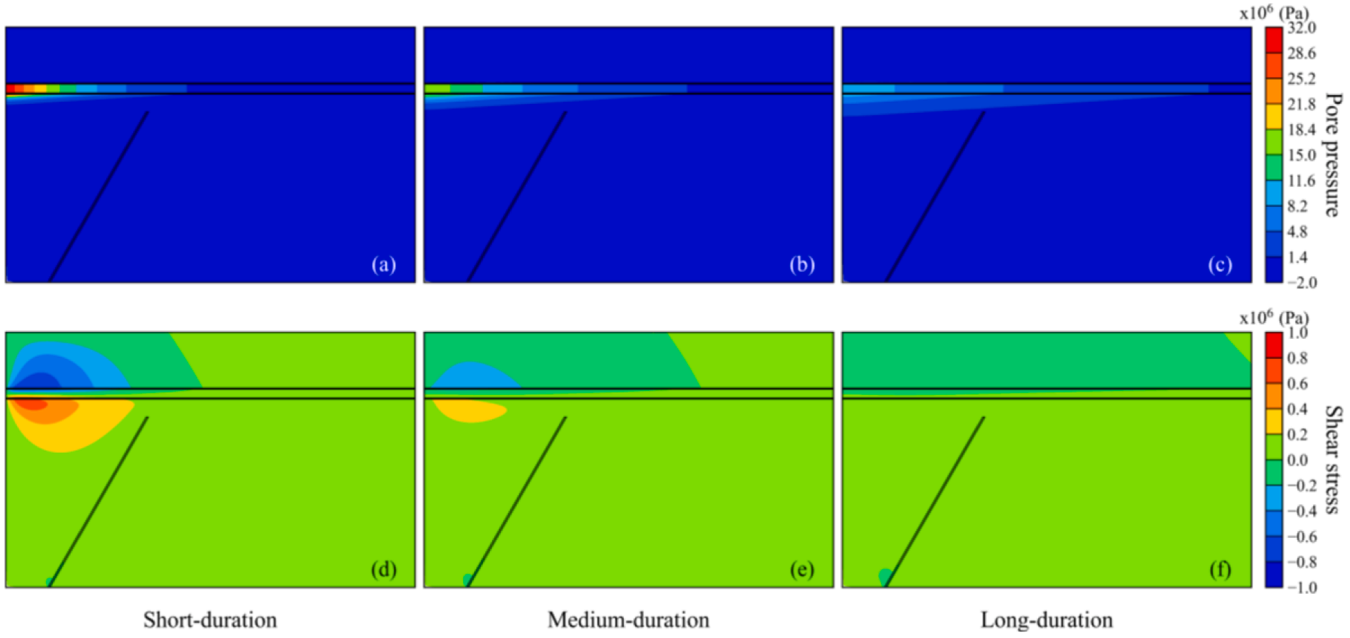


Fig. 7. End-of-injection distributions of the pore-pressure change Δp (a–c) and of the shear stress change (d–f) in the x–z section, for the sealing and isolated-fault configuration; on the two horizontal contacts the resolved shear stress change $\Delta\tau s$ equals the plotted $\Delta\sigma xz$. Panels (a, d), (b, e) and (c, f) are the short- (10 days), medium- (30 days) and long-duration (90 days) injection protocols, each delivering the same total injected mass. Panels within a row share a single colour scale, −2–32 MPa for Δp and −1–1 MPa for $\Delta\sigma_{xz}$, so that the three protocols can be compared directly rather than through three different colour bars. The thin horizontal lines mark the reservoir–caprock contact ($z = 100$ m) and the reservoir–basement contact ($z = 0$) and the heavy line marks the trace of the isolated fault.

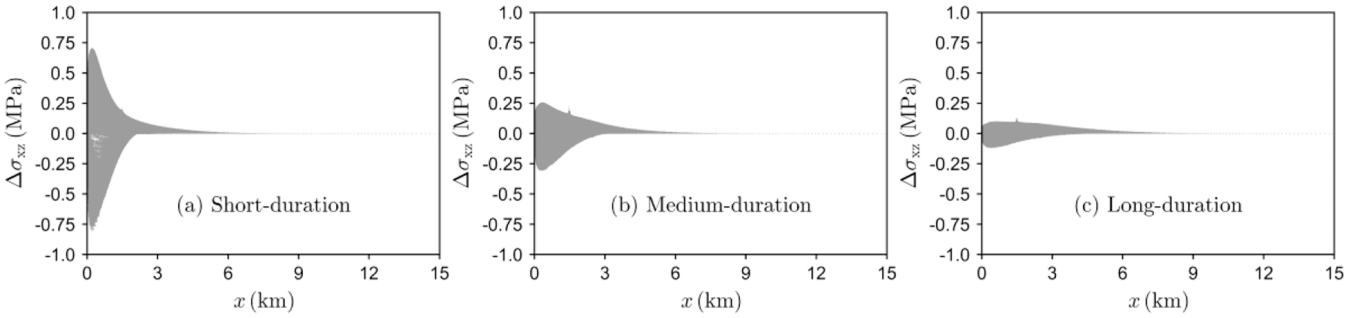


Fig. 8. Shear stress component change $\Delta\sigma_{xz}$ across the entire x–z section at the end of the injection phase of each protocol for the sealing and isolated-fault configuration, with (a) short- (10 days), (b) medium- (30 days) and (c) long-duration (90 days) injection, each delivering the same total injected mass. Every point is one mesh node of the section, plotted at its horizontal position x, so that the dense overlap of the points at a given x forms the shaded envelope; its vertical extent at each x is the variation of $\Delta\sigma_{xz}$ over depth at that location. The envelope is widest in the immediate vicinity of the injection boundary ($x \to 0$) and decays to near zero within the first few kilometres; at fixed injected mass, the peak magnitude decreases as the injection duration lengthens.

Because slip tendency is controlled by Coulomb stress rather than shear stress alone, Fig. 9 decomposes the stress and pressure contributions at the end of the injection, for each of the three protocols, with $f = 0.5$. The separated fields emphasize that ΔCFS depends on the combined contributions of interface-parallel shear loading, normal stress modulation, and pore pressure reduction of effective normal stress, and they make the relative weight of the three contributions explicit. The peak Δp at the well is 10–32 MPa across the three protocols against a resolved shear stress change of at most 0.9 MPa, so the Coulomb loading on these contacts is carried predominantly by the pore-pressure term. The two contacts share almost identical Δp and $\Delta\sigma_n$ profiles, because the sealed reservoir transmits the pressure change to both boundaries almost equally. They differ in $\Delta\tau_s$, where the reservoir–caprock contact carries the larger local peak at every duration (0.85, 0.32 and 0.12 MPa against 0.67, 0.22 and 0.07 MPa) while the reservoir–basement contact carries the broader footprint. The resulting ΔCFS patterns along the two interfaces (Fig. 9d, e, i, j, n, o) show the same ordering as the shear loading. The reservoir–basement contact develops the broader Coulomb-loading footprint at every duration, 3.62, 4.79 and 6.96 km against 2.59, 4.15 and 6.58 km for loading above 0.05 MPa, even though its shear-stress peak is slightly lower. Comparing the rows also quantifies the peak-footprint trade-off. As the injection lengthens, the peak ΔCFS on the reservoir–basement contact falls from 10.7 to 5.9 to 3.3 MPa while its footprint grows from 3.6 to 4.8 to 7.0 km.

These perturbations translate into distinct spatiotemporal patterns of the relative seismicity-rate indicator $R(t)$ (Fig. 10). At injection termination (vertical dashed lines), protocol-dependent differences in peak and persistence are apparent. Short-duration injection produces the highest rate at shut-in, with $\log_{10}R \approx 5.5$ at the end of 10 days, reflecting the most intense near-well stressing pulse. Medium-duration injection maintains a high activity level at shut-in, with $\log_{10}R > 4$ at 30 days, reflecting sustained stress change during injection and slower decay after termination. Long-duration injection produces a lower peak at shut-in ($3 < \log_{10}R < 4$ at 90 days), consistent with gradual accumulation under prolonged low-rate loading and incomplete stress relaxation by the time injection ends. This peak-footprint-persistence trade-off

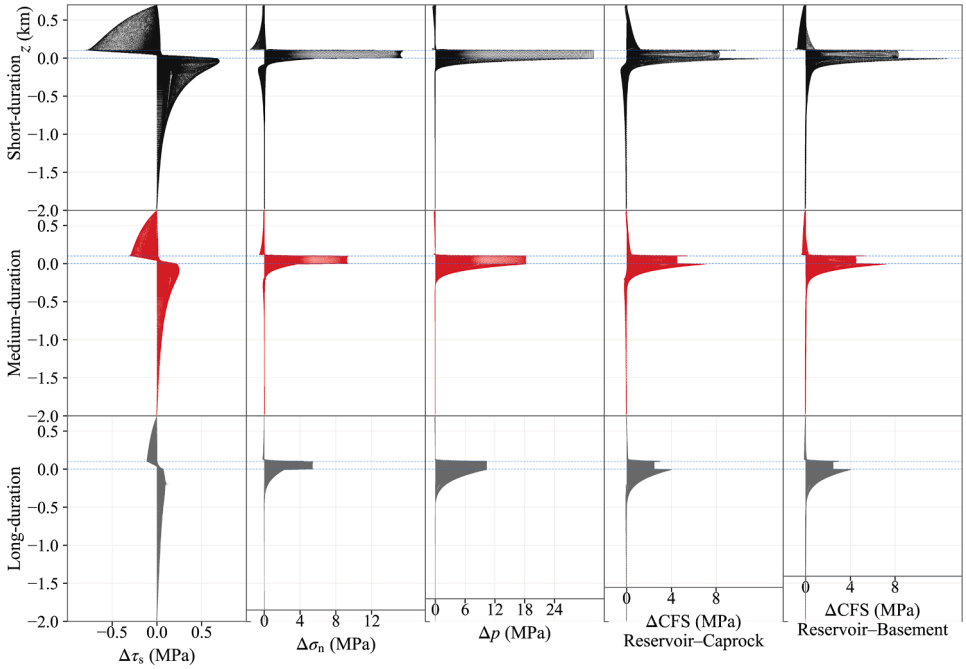


Fig. 9. Decomposition of the hydro-mechanical perturbation at the end of injection for the sealing and isolated-fault configuration. The rows are the short- (10 days), medium- (30 days) and long-duration (90 days) injection protocols, each delivering the same total injected mass; the columns are, from left, the interface-resolved shear stress change $\Delta\tau_s$, the normal stress change $\Delta\sigma_n$, the pore pressure change Δp, the Coulomb failure stress change ΔCFS on the reservoir–caprock contact, and the corresponding ΔCFS on the reservoir–basement contact. At every depth z the shading spans the range of the quantity along the horizontal line at that depth, so that the width of the shading at each z is the spread of the quantity across the x–z section; panels within a column share a common horizontal scale. The horizontal dashed lines mark the two contact depths ($z = 0$ and $z = 100$ m). The friction coefficient is $f = 0.5$.

has an important operational implication. A lower peak pressure does not necessarily imply a smaller affected region or a shorter monitoring window. Long-duration injection may limit near-well pressure buildup, but it can broaden the region experiencing favorable Coulomb loading and prolong the post-shut-in period over which elevated loading persists. Injection protocols in layered reservoirs should therefore be compared using both peak-response and persistence-based criteria.

The post-injection duration of the elevated relative rate response also scales strongly with injection duration. In the $\mu^* = 0$ limit, where the response is driven by $\Delta\tau_s$ alone and the elevated window is finite, the interval over which the contact rate exceeds twice its background value lengthens with injection duration, 64, 75 and 114 days on the reservoir–caprock contact and 77, 87 and 122 days on the reservoir–basement contact for the short, medium and long protocols. At $\mu^* = 0.5$ the same threshold is exceeded to the end of the 300-day window in every case. This scaling shows that long-duration injections can reduce peak stressing intensity but extend the duration of elevated secondary seismicity-rate response by maintaining positive or slowly evolving Coulomb failure stress change over longer times and larger distances. This effect is especially pronounced along the reservoir–basement interface, where indirect poroelastic stressing dominates in the absence of direct hydraulic connectivity. Repeating the μ^* sweep for all three protocols separates the two controls (Fig. 6c). At fixed μ^* the interface rate response falls by roughly an order of magnitude for each step in injection duration. At $\mu^* = 0.5$ the peak rate on the reservoir–caprock contact is 2.6×10^6, 3.0×10^5 and 3.3×10^4 for the short, medium and long protocols, whereas the fault response is essentially the same in all three (1313, 1310 and 1263 at $\mu^* = 0.5$; 11.3, 11.3 and 11.1 at $\mu^* = 0$). The reason is that with equal injected mass the peak forcing at the fault is the same in all three protocols, the peak $|\Delta S|$ being 0.280, 0.280 and 0.278 MPa. The fault is fed through the conductive pathway by the total mass, rather than by the injection rate. What the protocol changes at the fault is therefore not the amplitude of the rate response but its timing. The time of the peak moves from 88 to 99 to 137 days as the injection duration increases. The fixed-mass simulations therefore show a clear trade-off. Short, high-rate injection concentrates large near-field stressing and produces sharp early peaks, whereas longer, lower-rate injection broadens the footprint and prolongs the elevated relative rate response, particularly along the basement interface.

Primary fault-related loading along a reservoir-crossing fault

To quantify the injection-induced stress change of a reservoir-associated fault, we separate the relative roles of (*i*) direct hydraulic loading through pore pressure diffusion and (*ii*) indirect poroelastic stressing transmitted through the surrounding rock matrix. To this end, we evaluate Coulomb failure stress change along the fault both excluding the pore pressure contribution (poroelastic stressing only) and including the full Coulomb formulation with the $f \cdot \Delta p$ term (Fig. 11). For the conductive and crossing fault configuration, pore pressure preferentially migrates downward within the fault zone, which acts as a high-permeability pathway ($k = 1.0 \times 10^{-13}$ m^2 in the conductive case). By 100 days after injection initiation (within the 300-day simulation period), this hydraulic connection produces substantial pore pressure elevation within and near the fault (Fig. 11a) and, consequently, elevated Coulomb stress along the fault plane when pore pressure effects are included (Fig. 11c). Beyond the direct $f \cdot \Delta p$ contribution, poroelastic stressing alone also increases fault slip tendency (Fig. 11b), reflecting propagation of shear and normal stress perturbations through the stiff basement. This behavior is consistent with poroelastic fault analyses by Chang and Segall,[11] which show that basement faults may experience increased Coulomb loading through indirect poroelastic stress transfer even outside the primary pore-pressure plume.

All fault quantities reported in Section 3 are computed by resolving the full stress tensor onto the fault plane as described in Section 2.2, rather than from a single shear component. Fig. 12 has nine panels. Panels (a–c) show the pore-pressure change Δp along the fault at shut-in, 100 days and 300 days; panels (d–f) show the poroelastic contribution to

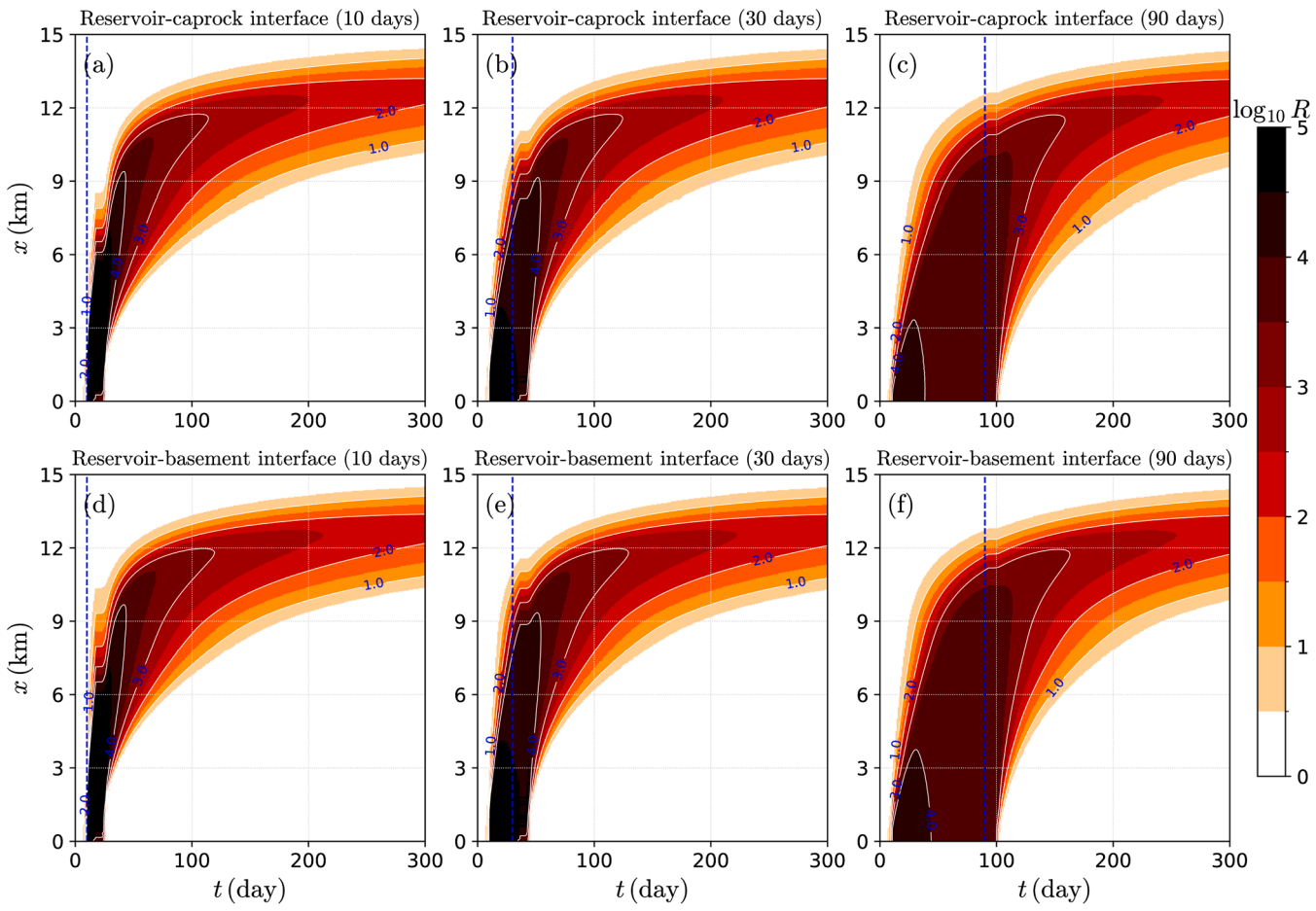


Fig. 10. Relative seismicity-rate indicator $R(t)$ along the stratigraphic interfaces for the sealing and isolated-fault configuration, computed with $\Delta S = \Delta\tau_s - \mu^*(\Delta\sigma_n - \Delta p)$ at $\mu^* = 0.5$ (the conventional, critically stressed end-member; Fig. 6), with (a–c) reservoir–caprock interface and (d–f) reservoir–basement interface under short- (10 days), medium- (30 days), and long-duration (90 days) injection protocols, respectively. Vertical dashed lines mark shut-in for each protocol.

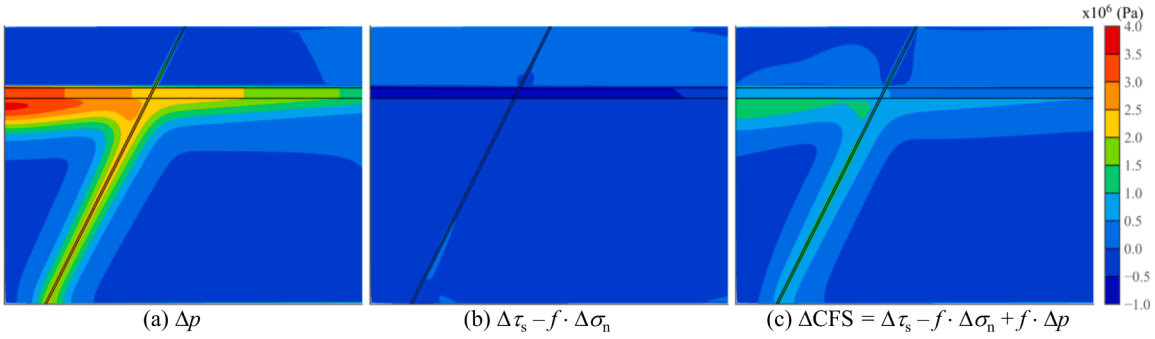


Fig. 11. Fault response for the medium-duration injection case (30 days) with a conductive, reservoir-crossing fault, shown at $t = 100$ days within the 300-day simulation period. (a) Pore-pressure change. (b) The poroelastic contribution to the Coulomb failure stress change, $\Delta\tau_s - f\,\Delta\sigma_n$. (c) The total Coulomb failure stress change, $\Delta\tau_s - f\,\Delta\sigma_n + f\,\Delta p$, with $f = 0.5$. All three panels share a single colour scale, −1–4 MPa, so that the relative weight of the three contributions is visible directly. The pore-pressure change reaches 3.64 MPa at the well whereas the poroelastic contribution stays within ±0.95 MPa, so the Coulomb loading on the conductive fault is carried predominantly by the pore-pressure term.

the Coulomb failure stress change, $\Delta\tau_s - f\,\Delta\sigma_n$, at the same three times; and panels (g–i) show the total Coulomb failure stress change ΔCFS, including the pore-pressure term, at the same three times. Panels within each row share a common colour scale, which shows directly that the pore-pressure contribution dominates the total Coulomb loading on the conductive fault.

To assess the influence of injection protocol, Fig. 12 compares Coulomb stress distributions along the fault for short-, medium-, and long-duration injections with the same total injected mass, computed both without (Fig. 12d-f) and with (Fig. 12g-i) the pore pressure term. At injection termination (Fig. 12d), poroelastic stressing produces a peak in Coulomb stress near the reservoir-fault intersection and decays away from the overlap. In the short-duration, high-rate case, peak values are minimal because fluid diffusion remains confined near the injection boundary ($x \approx 1.6$ km from the fault), such that fault loading is dominated by poroelastic transfer rather than direct pressure diffusion

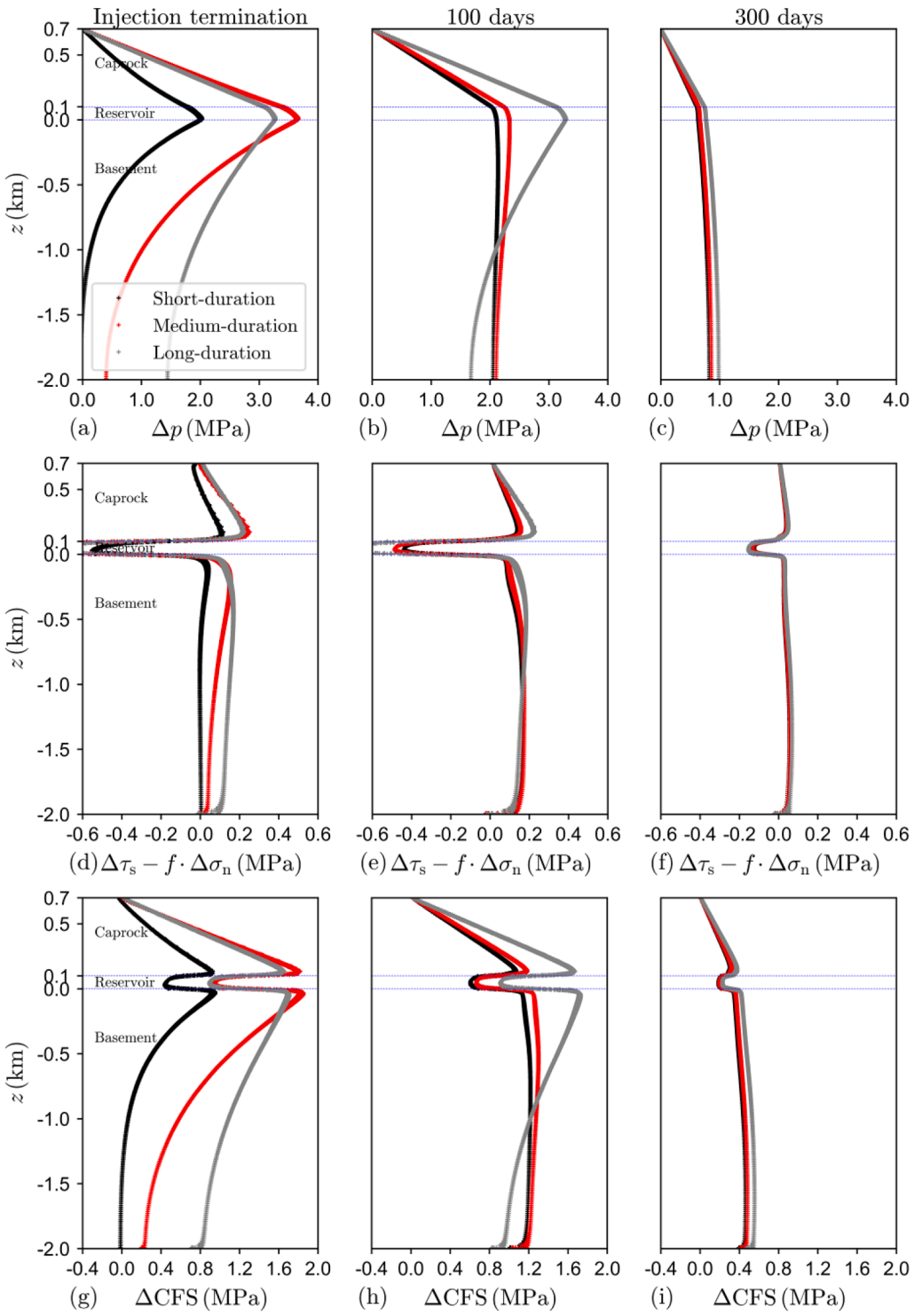


Fig. 12. Coulomb failure stress change along the fault, with the pore-pressure change Δp (a–c), the poroelastic contribution to the Coulomb failure stress change, $\Delta\tau_s - f\,\Delta\sigma_n$ (d–f), and the total Coulomb failure stress change ΔCFS (g–i) at injection termination, 100 days and 300 days. Panels within each row share a common colour scale. The black, red and grey lines denote the short-, medium- and long-duration injection scenarios, respectively. The horizontal dashed lines mark the stratigraphic interfaces and the labels identify the caprock, reservoir and basement.

(Fig. 12 g), with near-zero values along the deeper basement segment. In contrast, the long-duration, low-rate case exhibits higher Coulomb stress at shut-in because diffusion into the fault has already progressed prior to termination, yielding a more gradual decline with depth. The medium-duration case produces the highest peaks, consistent with more concentrated pressure buildup over the reservoir-fault crossing zone.

Post-injection evolution further highlights the interplay between connectivity and diffusion time. At $t = 100$ days after injection onset (Fig. 12 h), the short- and medium-duration cases approach a nearly uniform Coulomb stress of approximately 1.2 MPa along the basement fault plane, consistent with progressive filling of the conductive pathway and partial equilibration of pressure and stress. The long-duration case, however, still shows a systematic decline toward the basement at 100 days because only 10 days have elapsed since the end of

the 90-day injection, leaving insufficient time for full post-shut-in diffusion and stress redistribution. By $t = 300$ days (Fig. 12i), all protocols converge toward an approximately uniform Coulomb stress of approximately 0.5 MPa along the basement fault, indicating long-term poroelastic relaxation and diffusive equilibration of the coupled system.

Collectively, the simulations indicate that fault stressing reflects the interplay of (*i*) the injection timescale relative to diffusion, (*ii*) the injector-fault separation that controls perturbation travel time to the fault, and (*iii*) the duration of the post-injection period that controls equilibration. From an operational standpoint, short, high-rate injections tend to produce a response dominated by poroelastic stressing because pore pressure diffusion has insufficient time to hydraulically communicate with the fault. In contrast, longer injections allow pressure to penetrate conductive fault pathways prior to shut-in, increasing the direct $f \cdot \Delta p$ contribution and extending the interval over which the deeper fault segment experiences elevated Coulomb loading. For site screening, these results suggest that mapped faults should not be evaluated by injector-fault distance alone. Hydraulic connectivity, intersection with stratigraphic interfaces and the position of the fault relative to pressure-diffusion pathways together determine whether loading occurs mainly during injection or after shut-in. A fault segment that appears weakly loaded at shut-in may still become relevant later if diffusion and poroelastic stress transfer progressively engage the connected fault-interface network.

Spatiotemporal migration of the relative seismicity-rate response

We next examine how prescribed interface transmissivity growth modifies the migration of Coulomb loading and the associated relative seismicity-rate response. The analysis focuses on the medium-duration injection case with a conductive reservoir-crossing fault. Interface transmissivity growth is prescribed 5 days after injection onset and represented as rapid hydraulic enhancement, implemented as a four-order-of-magnitude permeability increase within the injection-side segments of the interface zones (the segments between the injection boundary and the fault). Because this change is imposed rather than solved from a slip or damage criterion, the results are interpreted as a sensitivity test of pathway reorganization. Fig. 13 shows that, without prescribed interface transmissivity growth, Coulomb stress along the reservoir–basement interface increases progressively during the 30-day injection period and continues to migrate laterally toward and past the fault during shut-in as poroelastic stresses diffuse and the pressure field equilibrates. In contrast, interface transmissivity growth produces a distinctly nonuniform stress evolution. By day 6, Coulomb stress decreases near the injection boundary due to enhanced drainage, while a pronounced stress peak emerges prematurely at the fault-interface intersection. This simultaneous near-field relaxation and intersection focusing indicates that migration is no longer governed solely by gradual diffusion distance; rather, once interface transmissivity increases, the coupled fault-interface network redirects the perturbation pathway and concentrates loading at the structural crossing zone.

Fig. 13 has eight panels, showing the evolution of the ΔCFS profile along the reservoir–basement interface at 1, 5, 6, 15, 30, 31, 100 and 300 days in reading order. The first two show the pre-growth state, the third the first output after the prescribed transmissivity increase, the next three the response over the remaining injection interval, and the last two the post-shut-in evolution. The fault–interface intersection is marked by a vertical dashed line in every panel, and a legend identifies the intact-interface and transmissivity-growth cases. The pronounced step in the ΔCFS profile that is visible where the profile crosses the fault is a feature of the model construction rather than a numerical artefact. The fault is an explicitly resolved body that, relative to the interface zone it crosses, is two orders of magnitude more permeable and substantially more compliant than the adjacent formations, so it decouples the two

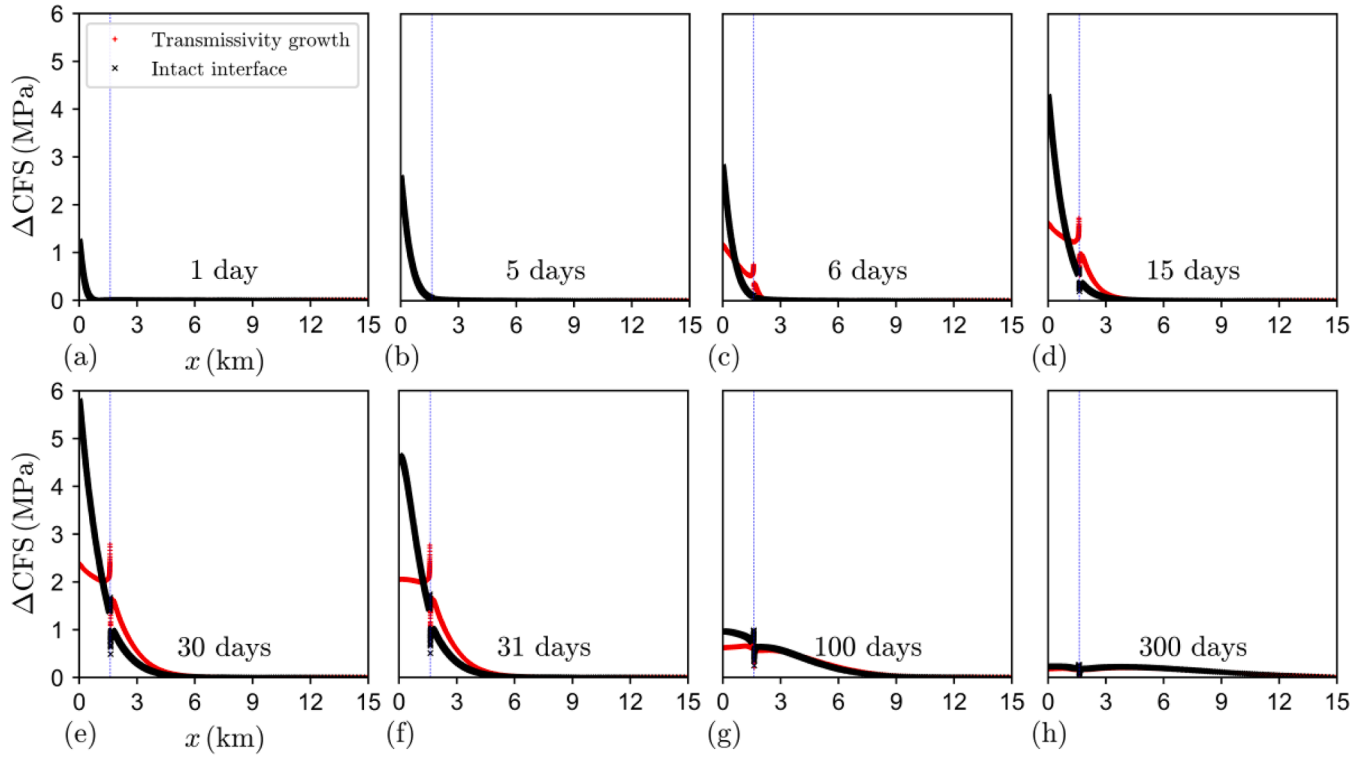


Fig. 13. Distributions of Coulomb failure stress change along the reservoir–basement interface for the medium-duration injection scenario with a conductive and crossing fault. Two cases are included, one (red line) with prescribed interface transmissivity growth (occurring at 5 days of injection) and the other (black line) without. For both cases, injection terminates at day 30, followed by a shut-in period extending to day 300. Results are obtained at 1, 5, 6, 15, 30, 31, 100, and 300 days of loading. The vertical dashed line marks the fault–interface intersection, where the interface element set is interrupted over the horizontal extent of the fault zone, so that the profile is not continuous across it.

segments of the interface. The interface element sets are interrupted over the 20 m horizontal extent of the fault, and the sampled profile therefore steps across it. The step appears at the same location with a comparable magnitude in the intact-interface case, where no interface permeability enhancement is applied, so it is not caused by the prescribed transmissivity increase. It is also not the along-interface gradient sampled across the gap. Resampling the same profile at the same 20.7 m spacing elsewhere on the interface gives differences that only rarely exceed 0.35 MPa at day 30, against a step of 1.62 MPa at the fault. The ratio of the two is 4–6 across all cases and times, and the profile is smooth on each side of the gap. It also responds to the fault-zone material and not to the mesh. In a five-case study in which only the fault material is varied, the step at day 30 changes from 1.62 MPa in the reference case to 2.03, 3.18 and 5.56 MPa as the fault permeability is reduced by factors of ten and then a hundred. It becomes 2.29 MPa when the fault stiffness alone is changed. The response therefore varies by a factor of 3.4 in a model whose mesh is identical, node for node, in all five runs. The physical character of the step changes with the fault's hydraulic role. While the fault is more permeable than the units it separates, the pore pressure is continuous across it and the step is carried by the resolved tractions. A fault as tight as the basement instead becomes a pressure barrier, and the pore pressure itself steps, by 12.5 MPa. Finally, the step survives the removal of the material contrast along the interface. When the fault material is replaced by the material of the interface it crosses, the sampled mid-plane carries no material discontinuity at all. The step nevertheless does not vanish but grows to 2.62 MPa at day 30, 2.6 times the reference value. The two properties changed by that substitution act independently and additively. The mechanical properties alone (stiffness, Poisson's ratio, density, porosity, Biot coefficient and storage, with the permeability left unchanged) give 1.62 MPa and the permeability alone gives 1.98 MPa, against 0.99 MPa in the reference. The combined effect matches the sum of the two individual contributions ($1.62 + 1.98 - 0.99 = 2.61$ MPa against 2.62 MPa computed). The two mechanisms are distinguishable in the fields. The mechanical substitution leaves the pore pressure continuous across the zone (0.04 MPa) and enlarges the normal-traction contribution from 0.22 to 0.79 MPa. The hydraulic substitution turns the fault into a barrier, so that the pressure itself steps by 2.10 MPa and the traction contribution collapses to 0.05 MPa. The step is therefore controlled by the fault body's stiffness and by its hydraulic role, neither of which can be matched to both of the units that the contact separates. Across the ten material assignments we have run on this single mesh, six on the transmissivity-growth configuration and four on the intact one, the day-30 step ranges from 0.99 to 5.56 MPa. The reference fault-zone parameters give the smallest step of any assignment tested, and in every case the step remains several times larger than the ordinary 20.7 m resampling differences on the same interface. The step is a prescribed-material feature of a model in which the fault zone is explicitly resolved.

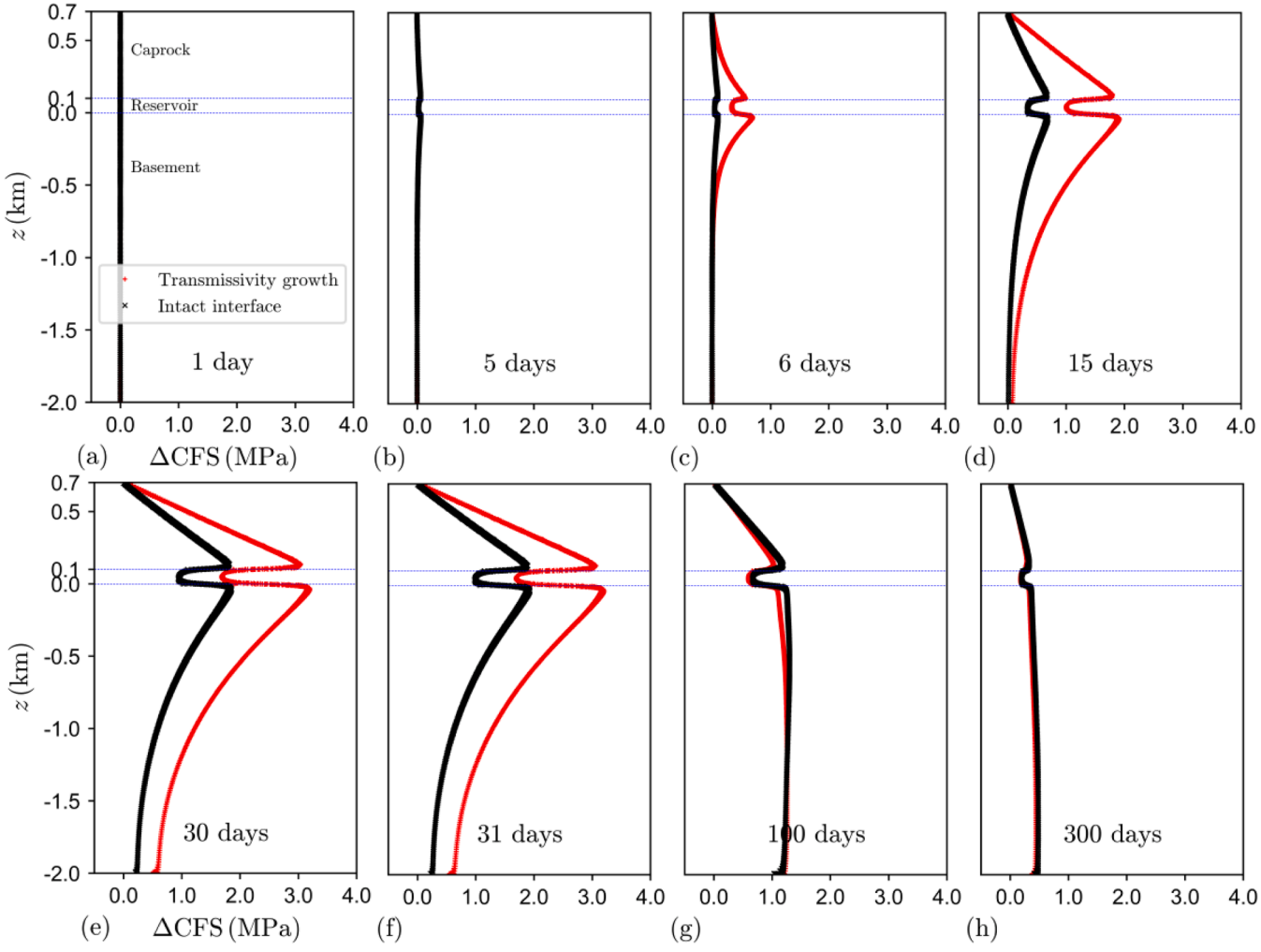


Fig. 14. Distributions of Coulomb failure stress change along the fault for the medium-duration injection scenario with a conductive and crossing fault. Two cases are included, one (red line) with prescribed interface transmissivity growth (occurring at 5 days of injection) and the other (black line) without. For both cases, injection is completed at 30 days, and post-injection is applied up to 300 days. Results are obtained at 1, 5, 6, 15, 30, 31, 100, and 300 days of loading. The shaded bands mark the two stratigraphic contacts (the reservoir–basement contact at $z = 0$ and the reservoir–caprock contact at $z = 100$ m).

Fault stressing accelerates markedly in the prescribed interface-transmissivity-growth case (Fig. 14). The fault's rate response crosses twice its background value about a day earlier than in the intact-interface scenario (day 5.2 against day 6.0), and the Coulomb stress reaches substantially larger magnitudes near the reservoir intersection. Quantitatively, by day 15, the prescribed interface-transmissivity-growth case exhibits peaks exceeding 2 MPa near the intersection; by day 30, the enhanced stressing propagates deeper into the basement, whereas the intact-interface case remains comparatively delayed and subdued. Importantly, the divergence persists after injection termination. During 31–300 days, the prescribed interface-transmissivity-growth scenario maintains systematically higher stress levels, consistent with sustained hydraulic connectivity that facilitates faster pressure redistribution and stronger poroelastic coupling along the fault plane.

The corresponding relative seismicity-rate fields (Fig. 15) show that prescribed interface transmissivity growth also changes the temporal structure of fault loading. In the intact-interface case, elevated $R(t)$ persists over a relatively broad window of approximately 162 days, consistent with diffusion-controlled stressing and gradual post-injection relaxation. With prescribed interface transmissivity growth at day 5, the strongest rate increases become concentrated within approximately 20–60 days, reflecting accelerated stress transfer and a more impulsive loading history near the fault-interface intersection. These results indicate that prescribed interface transmissivity growth can shift the response from gradual diffusion-dominated loading toward focused intersection-controlled loading. This pathway-reorganization effect is relevant for risk monitoring because near-well pressure relaxation and far-field loading concentration can occur simultaneously. A pressure decrease near the injector after interface transmissivity enhancement should therefore not be interpreted automatically as a system-wide reduction in loading. Monitoring strategies based only on well pressure or near-well response may miss the development of focused loading along connected stratigraphic interfaces and fault intersections.

Discussion

Stress-history control of injection-induced Coulomb loading

In layered reservoirs, injection-induced Coulomb loading is better viewed as a stress-history problem than as a response to peak pressure alone. Holding injected mass constant while varying injection duration highlights how the temporal distribution of forcing shapes Coulomb-loading trajectories on discontinuities. In the relative rate framework used here, $R(t)$ responds to the time evolution of Coulomb failure stress change and stressing rate, rather than to a single peak pressure or shut-in value. Thus, changing injection duration modifies more than the peak pressure response. It also changes where, when, and for how long discontinuities remain under positive Coulomb loading after shut-in.

Fault loading in such systems is conditioned by hydraulic connectivity and by the time required for pressure and stress perturbations to traverse geometric offsets. Conductive faults can enhance direct hydraulic loading along the fault zone, whereas poroelastic stress transfer can elevate Coulomb failure stress change beyond the main pressure plume, expanding the region where Coulomb loading may increase.[13] This perspective explains why shut-in does not necessarily mark the end of elevated loading. A weak fault response at shut-in may indicate that the coupled pressure and stress perturbations have not yet reached the fault, whereas longer injections may load the fault earlier by allowing diffusion and poroelastic stress transfer to reach the reservoir-fault overlap zone during injection.

Stiffness-contrast and boundary-condition controls

To separate the causes of the asymmetry between the two contacts, four control configurations were run (Fig. 16, Table 4), each identical to the reference model except in one respect. C2 equalizes the caprock and basement moduli (both 44.95 GPa). C3 replaces the free surface with a roller while keeping the imposed hydraulic boundary conditions unchanged, so that the top boundary remains drained and only the mechanical asymmetry is removed, and C4 combines the two changes. All four configurations ran to the full 90-day window and were post-processed identically. At shut-in the peak ΔCFS is 5.395 MPa on the upper and 5.901 MPa on the lower contact in C1; 5.435 and 5.945 MPa in C2; 5.949 and 6.453 MPa in C3; and 5.938 and 6.445 MPa in C4, with footprints (the along-contact length over which $|\Delta CFS|$ exceeds 0.05 MPa) of 4.15/4.79 km, 4.15/4.79 km, 4.53/4.93 km and 4.62/4.84 km respectively. Removing the stiffness contrast leaves the peak ΔCFS essentially unchanged (5.435 and 5.945 MPa in C2 against 5.395 and 5.901 MPa in C1) and the footprints identical (4.15 and 4.79 km in both), although the shear-stress peaks change by up to 0.04 MPa and the fault rate falls from 8.1 to 5.6. The stiffness contrast is therefore not the cause of the asymmetry. Making the top boundary a roller raises the peak ΔCFS to 5.949 and 6.453 MPa and widens the footprints to 4.53 and 4.93 km, but leaves the lower-over-upper peak ratio essentially unchanged (1.094 in C1, 1.085 in C3). Combining both changes reproduces C3, so the moduli contribute no further effect. The residual asymmetry therefore survives both manipulations and is associated with the hydraulic boundary asymmetry of the model, a drained top and a no-flow bottom, which was deliberately held fixed in all four configurations. On the fault, the peak relative rate is likewise insensitive to the stiffness contrast ($R_{max} = 8.1$ in C1 against 5.6 in C2), but it is amplified about thirty-fold by the mechanical boundary change ($R_{max} = 251$ in C3 and 242 in C4, both peaking at shut-in and decaying afterwards). It follows the higher peak fault shear-stress change through the

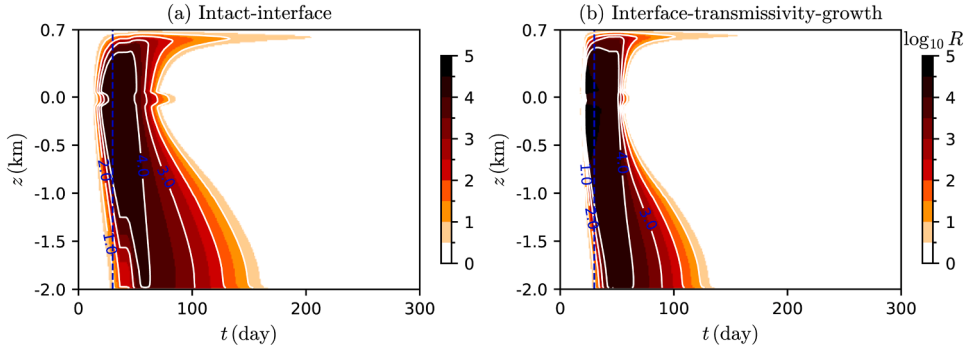


Fig. 15. Relative seismicity-rate indicator $R(t)$ resolved along the fault under the medium-duration injection scenario with a conductive reservoir-crossing fault, with (a) intact interface and (b) prescribed interface-transmissivity growth, initiated at day 5. The vertical dashed line marks injection termination at day 30. The rate is obtained from the resolved shear stressing history with the same integrator used for the μ^* sweep of Section 2.5 and Fig. 6; the elevated response is confined to about 130 days after shut-in in both cases and decays earlier at depth in the growth case.

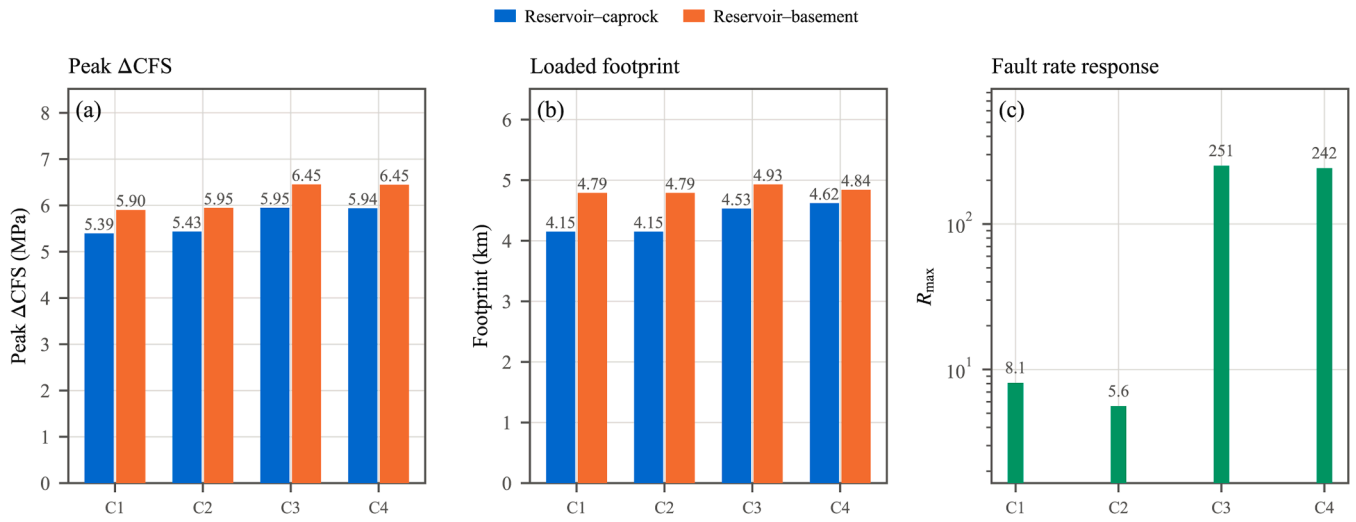


Fig. 16. Boundary-condition and stiffness control experiments. Peak ΔCFS (a) and loaded footprint (b) on the two interfaces at shut-in, and the fault rate response (c), for the four configurations of Table 4. Removing the stiffness contrast (C2) leaves the peak ΔCFS essentially unchanged (5.435 against 5.395 MPa on the reservoir–caprock contact and 5.945 against 5.901 MPa on the reservoir–basement contact) and the footprints identical, although the shear-stress peaks change between the two contacts; replacing the free surface with a roller (C3, C4) raises the peaks to 5.949 and 6.453 MPa and the fault R_{max} by a factor of 30 ($\mu^* = 0$).

Table 4
Boundary-condition and stiffness control experiments (30-day injection protocol, $f = 0.5$). Peak values at shut-in; footprint = the along-contact length over which $|\Delta CFS|$ exceeds 0.05 MPa. The fault metrics are maxima over the first 90 days. C2 equalizes the caprock and basement moduli (44.95 GPa); C3 replaces the free surface with a roller; C4 combines both changes.

Quantity	C1 (reference)	C2 (equal moduli)	C3 (top roller)	C4 (both)
Caprock / basement moduli	Table 2	equal	Table 2	equal
Top / bottom mechanical BCs	free surface / roller	free surface / roller	roller / roller	roller / roller
Reservoir–caprock contact, peak $\Delta\tau_s$ (MPa)	0.323	0.360	0.253	0.284
Reservoir–basement contact, peak $\Delta\tau_s$ (MPa)	0.224	0.206	0.312	0.258
Reservoir–caprock contact, peak $\Delta\sigma_n$ (MPa)	7.58	7.50	6.65	6.66
Reservoir–basement contact, peak $\Delta\sigma_n$ (MPa)	6.51	6.41	5.60	5.59
Reservoir–caprock contact, peak ΔCFS (MPa)	5.395	5.435	5.949	5.938
Reservoir–basement contact, peak ΔCFS (MPa)	5.901	5.945	6.453	6.445
Reservoir–caprock contact, footprint (km)	4.15	4.15	4.53	4.62
Reservoir–basement contact, footprint (km)	4.79	4.79	4.93	4.84
Fault R_{max} (conventional)	1188	908	1685	1576
Fault R_{max} ($\mu^* = 0$)	8.1	5.6	251	242

exponential sensitivity of the rate-and-state response.

The same comparison was extended to a reference configuration in which the interface zones are removed altogether and the caprock, reservoir and basement are placed in direct contact, with everything else unchanged. Removing the interface zones raises the peak ΔCFS on the reservoir–basement contact from 5.901 to 7.410 MPa and leaves the reservoir–caprock peak essentially unchanged (5.395 against 5.462 MPa). The shut-in mean loading falls on the upper contact (1.71–1.16 MPa) and rises on the lower (1.91–2.40 MPa). The difference field taken on the identical mesh exceeds 0.05 MPa over 4.1 km of the reservoir–caprock contact and 3.8 km of the reservoir–basement contact, and exceeds one tenth of the local peak over 2.2 km of the reservoir–caprock contact and 1.3 km of the reservoir–basement contact. The interface zones therefore act over a multi-kilometre extent, rather than only in the immediate vicinity of the well. On the fault the change is comparatively small (peak rate over the first 90 days 8.1–7.9, duration of elevated rate 66–63 days, time to peak 90–88 days). The interface signal is therefore carried by the contacts themselves, rather than by the fault. The relative loading of the two contacts is not deducible from the pressure field alone. The reservoir–basement contact develops a stronger and broader Coulomb-loading footprint than the reservoir–caprock contact under identical injection histories.

Sensitivity to interface thickness and interface properties

All configurations in this section were run to the full 150-day window and post-processed identically. The interface thickness was varied over 1 m, 5 m (reference), 20 m and 50 m (Fig. 17, Table 5), with the interface properties held at the values of Table 2 and the mesh refined so that each interface is resolved by at least two elements across its thickness. The zero-thickness contact discussed above is included for reference. At shut-in the peak ΔCFS falls monotonically with thickness, from 5.502 MPa (1 m) to 5.395 (5 m), 5.043 (20 m) and 4.422 MPa (50 m) on the upper contact and from 6.007 to 5.901, 5.550 and 5.032 MPa; the peak overpressure falls from 18.6 to 14.5 MPa, and the loaded footprint from 4.26 to 3.32 km on the upper contact and from 4.88 to 4.30 km on the lower. The sensitivity is monotone but modest. A tenfold increase in thickness (5 m to 50 m) lowers the peak Coulomb loading from 5.395 to 4.422 MPa on the upper contact and from 5.901 to 5.032 MPa on the lower. The lower-over-upper contrast (ratio 1.09–1.14) and the timing of the peak (shut-in) are preserved at every thickness. On the fault the peak rate over the first 90 days falls with thickness (R_{max} = 8.3, 8.1, 6.7 and 5.1 for 1, 5, 20 and 50 m). The interface properties were then varied one at a time, independently of the averaging rule used to construct them. The interface stiffness was varied by factors of 0.5 and 2, and the interface permeability by factors of 0.1 and 10. Across these four variants the peak ΔCFS varies by at most 0.05 MPa (5.37–5.41 MPa on the upper contact, 5.87–5.91 MPa on the lower), the peak shear-stress change by at most 0.02 MPa, the footprint by at most 0.04 km, and the peak fault rate stays between 11.2 and 11.3. Neither the interface thickness nor the interface stiffness or permeability is therefore a first-order control on the modelled response over the

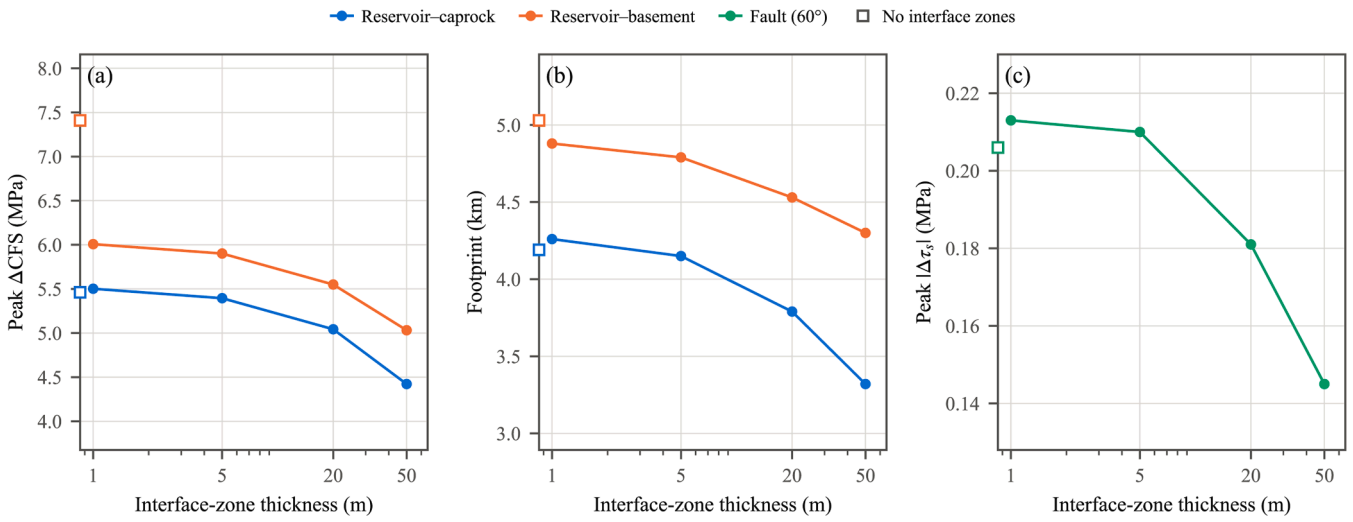


Fig. 17. Sensitivity to interface-zone thickness. Peak ΔCFS (a), loaded footprint (b) and peak fault shear-stress change (c) as functions of the interface thickness; the open square on the left axis of each panel is the configuration in which the interface zones are removed and the units are in direct contact.

Table 5
Sensitivity to interface-zone thickness and to removal of the interface zones (30-day injection protocol, $f = 0.5$). Peak values are taken at shut-in; the fault metrics are maxima over the first 90 days; the interface properties are held at the values of Table 2 throughout.

Quantity	1 m	5 m (reference)	20 m	50 m	removed (direct contact)
Reservoir–caprock contact, peak ΔCFS (MPa)	5.502	5.395	5.043	4.422	5.462
Reservoir–basement contact, peak ΔCFS (MPa)	6.007	5.901	5.550	5.032	7.410
Reservoir–caprock contact, footprint (km)	4.26	4.15	3.79	3.32	4.19
Reservoir–basement contact, footprint (km)	4.88	4.79	4.53	4.30	5.03
Fault peak $\lvert\Delta\tau_s\rvert$ (MPa)	0.213	0.210	0.181	0.145	0.206
Fault R_{max} (conventional)	1281	1188	621	187	1139
Fault R_{max} ($\mu^* = 0$)	8.3	8.1	6.7	5.1	7.9

ranges examined. The results are also insensitive to the choice between arithmetic and geometric averaging in constructing the interface properties. Taken together, these experiments show which inputs control the modelled response. It is insensitive to the interface stiffness and permeability over the ranges examined, modestly sensitive to the interface thickness, and strongly dependent on the injection history (Section 4.1) and on the boundary conditions (Section 4.2).

Stratigraphic-interface control of reservoir-fault loading pathways

Explicitly resolving thin stratigraphic interfaces changes the interpretation of the loading pattern because these contacts can behave as active hydro-mechanical elements rather than passive layer boundaries. In the layered-reservoir model of Chang and Segall,[11] the mechanical and hydraulic contrast at the reservoir–basement contact is imposed as a property jump, which carries no thickness, no storage and no independent strength. Seismicity there is evaluated on basement faults. Here the two contacts are explicit, finite-thickness hydro-mechanical zones with their own properties and their own response, evaluated as potential hosts of slip themselves rather than only as boundaries of the reservoir. The loading is quantified on the contacts as well as on the fault. These contacts coincide with sharp contrasts in stiffness, diffusivity, storage, and effective stress response, so the same injection protocol can generate different Coulomb-loading patterns across stratigraphic interfaces even when the reservoir pressure field appears similar. Because Coulomb failure stress change integrates shear loading, normal-stress modulation, and pore-pressure effects, interface loading tendency cannot be inferred from pressure diffusion alone, nor can it be reduced to pressure reaching a fault. In the present model, the reservoir–basement interface carries the broader Coulomb-loading footprint of the two contacts while the reservoir–caprock interface carries the larger local shear-stress change, and the asymmetry is not caused by the stiffness contrast between the units (Section 4.2). This result suggests that interface-related relative rate responses may provide diagnostic information on evolving stress-transfer pathways and on locations where subsequent fault loading may become concentrated.

The prescribed interface-transmissivity-growth simulations illustrate a pathway-modification mechanism that can alter diffusion-governed loading migration by enhancing perturbations near fault-interface intersections. Representing transmissivity growth as an abrupt permeability enhancement is an idealized end-member, but it isolates a physically plausible pathway in which hydraulic evolution along a stratigraphic contact can redirect perturbations and enhance Coulomb loading at structural intersections. Under this condition, the zone of highest loading potential need not coincide with the zone of highest reservoir pressure. It may instead develop near fault-interface intersections, where flow redistribution and poroelastic stress transfer are coupled. This interpretation is consistent with in situ injection experiments showing that slip and permeability changes along natural discontinuities can modify stress transfer and microseismic response, although the present model treats stratigraphic-interface transmissivity growth as a prescribed sensitivity case rather than a spontaneous slip process.[24] This loading focus at the fault–interface intersection requires the contact and the fault to be represented in the same coupled model.

Engineering implications and model limitations

The simulations have implications for site characterization, monitoring design, and injection management in layered reservoirs. For site characterization, the results indicate that reservoir–caprock and reservoir–basement contacts should be evaluated together with major faults. Their continuity, stiffness contrast, permeability contrast, and hydraulic

integrity can determine whether a stratigraphic contact behaves mainly as a barrier, a hydro-mechanical transfer zone, or a preferential pathway during injection. These interface properties therefore influence not only pressure diffusion within the reservoir, but also the location and persistence of Coulomb loading along stratigraphic contacts, adjacent fault zones, and fault-interface intersections.

For monitoring design, the results highlight fault-interface intersections as potential locations of focused loading. In the transmissivity-growth scenario, pressure relaxation near the injection boundary occurs together with enhanced Coulomb loading at the structural intersection. This indicates that a decline in near-well pressure should not automatically be interpreted as a reduction in system-wide loading. In layered reservoirs, pressure and stress perturbations may be redistributed from the injector vicinity toward more distant but structurally sensitive zones. Monitoring strategies should therefore integrate well pressure, microseismicity, deformation signals, and geological interpretation of interface continuity and fault connectivity, rather than relying only on near-well pressure response.

For injection management, the results show that the full loading history is more informative than peak pressure alone. At fixed injected mass, different injection durations produce different combinations of peak response, spatial footprint, and post-shut-in persistence. Short-duration injection favors stronger but more localized loading, whereas longer-duration injection can reduce the near-well peak while extending the affected region and prolonging positive Coulomb loading after shut-in. Shut-in decisions and post-injection surveillance should therefore consider both the timing and migration of pressure-stress perturbations. These findings suggest that stratigraphic contacts should be treated as part of the structural risk architecture of layered reservoirs, rather than as passive material boundaries used only for assigning hydraulic properties. This interpretation is consistent with studies showing that induced-seismicity control requires operational thresholds and monitoring criteria, that caprock stability depends on hydraulic-mechanical coupling and site-specific parameters, and that layered formations can modify injection-induced seismic moment release.[6–8,37]

These results should be interpreted as process-based screening outcomes rather than site-calibrated hazard predictions. Several assumptions limit direct field application. The interface rate responses are conditional on the assumed background stress state. As discussed in Section 2.5, a strictly horizontal, Andersonian contact has no sensitivity to pore-pressure change in this framework. The reported sensitivity to μ^* therefore represents the range of plausible contact dips rather than a calibrated in-situ state. Site-specific application requires the background stress state to be constrained, for example from borehole breakouts, focal mechanisms or in-situ stress measurements. The fault zone is treated as a homogeneous equivalent material rather than as a damage zone with internal structure, and the transmissivity-growth scenario is prescribed rather than computed from a hydromechanical failure criterion. The model assumes linear poroelasticity, piecewise homogeneous material properties, and a plane-strain configuration. It does not resolve nonlinear inelastic deformation, thermal or chemical effects, multiphase flow, or fully coupled slip-permeability feedback. The relative rate formulation is used only to map Coulomb stressing histories into a diagnostic rate response, not to simulate dynamic rupture, earthquake interactions, earthquake occurrence, or magnitude-frequency behavior. The timing and magnitude of interface transmissivity growth are also prescribed, so these scenarios should be viewed as controlled sensitivity tests of pathway modification rather than predictions of spontaneous interface failure.

The use of a single reference background stress state, and of a common rate-and-state parameter set for interfaces and faults, further limits the site-specific interpretation of absolute rate values; the μ^* sweep quantifies the sensitivity to that choice but cannot replace a site-specific stress state. In natural systems, frictional properties, effective normal stress, roughness, clay content, damage state, and hydraulic connectivity may vary substantially among faults and stratigraphic contacts. Future work should couple stress, slip, permeability evolution, and damage processes along interfaces and faults, and should extend the framework to fully three-dimensional fault-interface networks. Field monitoring data should also be used to constrain uncertainties in peak response, loading footprint, and post-shut-in persistence, so that process-based simulations can be incorporated into risk-informed injection design and monitoring strategies.

Not all of these conclusions depend on the choice of forcing function in the same way. The trade-off between peak response, footprint and persistence, the broader loading footprint of the reservoir–basement contact, the boundary-controlled rather than stiffness-controlled asymmetry between the two contacts, the dependence of fault loading on hydraulic connectivity and travel time, and the focusing of loading at the fault–interface intersection all follow from Δp and $\Delta\tau_s$. They therefore survive the $\mu^* = 0$ limit of the forcing function, in which the rate response is driven by $\Delta\tau_s$ alone. Only the numerical values of ΔCFS and of the relative rate indicator, and the ordering of the two contacts' rate response, depend on μ^*; they are reported across $\mu^* = 0$–0.5, over which the ordering of the two contacts reverses between $\mu^* = 0$ and $\mu^* = 0.1$.

Conclusions

This study examined how reservoir-bounding stratigraphic interfaces influence injection-induced Coulomb loading in a layered caprock–reservoir–basement system. The reservoir–caprock and reservoir–basement contacts were represented as finite-thickness hydro-mechanical interface zones, and their responses were compared with that of a reservoir-crossing fault. The analysis focused on pressure diffusion, poroelastic stress transfer, Coulomb failure stress change, and a Dieterich-type relative rate indicator. The rate indicator was used only as a diagnostic measure of time-dependent loading tendency, not as a simulation of spontaneous rupture or earthquake occurrence. The main conclusions are as follows.

1. Injection duration controls a trade-off among peak response, affected footprint, and post-shut-in persistence when the total injected mass is fixed. Short-duration, high-rate injection produces the strongest local loading pulse near the injection boundary, but the affected region remains limited. Longer-duration injection reduces the near-well pressure peak, but promotes broader pressure redistribution and longer persistence of positive Coulomb loading after shut-in. In the intact-interface cases, the interval over which the interface rate response exceeds twice its background value lengthens with injection duration at $\mu^* = 0$, from 64 to 114 days on the reservoir–caprock contact and from 77 to 122 days on the reservoir–basement contact between the 10-day and 90-day protocols. At $\mu^* = 0.5$ the same threshold extends to the end of the simulated window.
2. The reservoir–basement interface shows a stronger monitoring-relevant loading footprint than the reservoir–caprock interface. This asymmetry is a result of the differing boundary conditions and of the hydraulic contrast rather than of the stiffness contrast. Control experiments that remove the stiffness contrast leave the peak Coulomb loading essentially unchanged (within 0.05 MPa), while the residual lower-over-upper asymmetry is associated with the hydraulic boundary asymmetry. The asymmetry, and its sign, are preserved for all interface thicknesses examined (1–50 m) and for all interface stiffness and permeability variants. This difference is not caused by the stiffness contrast, which the control experiments show to have no material effect on it; it accompanies the hydraulic asymmetry between the drained top and the no-flow bottom of the model. The lower interface may not always show the largest local shear-stress peak, but it can transmit moderate Coulomb loading over a broader distance. This indicates that basement contacts should be considered as active hydro-mechanical transfer zones in layered reservoirs, especially where they intersect faults.

3. Fault loading depends on both hydraulic connectivity and the time required for pressure and stress perturbations to reach the fault. In the conductive fault case, longer injection allows pressure to enter the fault zone before shut-in, increasing the direct pore-pressure contribution to Coulomb loading. After shut-in, pressure diffusion and poroelastic stress redistribution can continue to load deeper fault segments. Thus, a weak fault response at shut-in does not necessarily indicate low post-injection loading potential.
4. Prescribed interface transmissivity growth changes the loading pathway by diverting hydraulic and poroelastic perturbations toward the fault-interface intersection. In this end-member scenario, enhanced transmissivity reduces pressure accumulation near the injection boundary, but the redistributed perturbation produces stronger Coulomb loading at the structural intersection. Compared with the intact-interface case, the fault begins to respond earlier, and Coulomb stress near the intersection exceeds 2 MPa by day 15. This result indicates that near-well pressure decline does not necessarily imply a reduction in system-wide loading. When a stratigraphic contact becomes more transmissive and is hydraulically or mechanically connected to a fault, loading may be transferred from the injector vicinity to a more distant but structurally sensitive zone.
5. For engineering geological assessment, layered-reservoir injection should be evaluated using structural and temporal criteria together. Site characterization should include the continuity, thickness, stiffness contrast, permeability contrast, and hydraulic integrity of reservoir-bounding contacts, as well as the geometry and connectivity of fault-interface intersections. Monitoring and injection management should consider not only peak well pressure and mapped faults, but also loading migration along stratigraphic interfaces and post-shut-in persistence.

The proposed framework is most useful as a process-based screening tool for identifying structural controls on injection-induced loading in layered reservoirs. Its direct field application requires site-specific constraints on stress state, interface properties, fault permeability, frictional behavior, and monitoring data. Future developments should incorporate nonlinear interface deformation, slip-permeability feedback, damage or dilation criteria, and fully three-dimensional fault-interface networks. These additions would improve the ability to connect pressure-stress transfer mechanisms with field-scale monitoring and risk-informed injection management.

CRediT authorship contribution statement

Shu-Gang Ai: Writing – original draft, Visualization, Validation, Software, Methodology, Funding acquisition, Conceptualization. **Ke Gao:** Writing – review & editing, Supervision, Project administration, Methodology, Funding acquisition, Conceptualization.

Declaration of Competing Interest

The authors declare that they have no known competing financial interests or personal relationships that could have appeared to influence the work reported in this paper.

Acknowledgments

This work was supported by the Shenzhen Science and Technology Program (JCYJ20250604144056051), the National Science and Technology Major Project of China (2024ZD1000400), and the Guangdong Basic and Applied Basic Research Foundation (2023A1515110593). The authors declare no conflicts of interest. AI tools were used only for minor language polishing.

Data availability

Data will be made available on request.

References

1. Ellsworth WL. Injection-induced earthquakes. *Science*. 2013;341, 1225942.
2. Häring MO, Schanz U, Ladner F, Dyer BC. Characterisation of the Basel 1 enhanced geothermal system. *Geothermics*. 2008;37:469–495.
3. Kaven JO, Hickman SH, McGarr AF, Walter S, Ellsworth WL. Seismic monitoring at the Decatur, IL, CO2 sequestration demonstration site. *Energy Procedia*. 2014;63:4264–4272.
4. Keranen KM, Savage HM, Abers GA, Cochran ES. Potentially induced earthquakes in Oklahoma, USA: Links between wastewater injection and the 2011 Mw 5.7 earthquake sequence. *Geology*. 2013;41:699–702.
5. Weingarten M, Ge S, Godt JW, Bekins BA, Rubinstein JL. High-rate injection is associated with the increase in US mid-continent seismicity. *Science*. 2015;348:1336–1340.
6. Chen B, Li Q, Tan Y, et al. Caprock sealing integrity and key indicators of CO2 geological storage considering the effect of hydraulic-mechanical coupling: X field in the Bohai Bay Basin, China. *Eng Geol*. 2024;342, 107741.
7. Cui ZD, Liu DA, Zeng RS, Niu JR, Wang HJ, Shi XS. Resistance of caprock to hydraulic fracturing due to CO2 injection into sand lens reservoirs. *Eng Geol*. 2013;164:146–154.
8. Lu D, Wu W. Injection-induced seismic moment in layered rock formations. *Eng Geol*. 2024;343, 107793.
9. Zhou X, Burbey TJ. Deformation characteristics of a clayey interbed during fluid injection. *Eng Geol*. 2014;183:185–192.
10. Cappa F, Rutqvist J. Impact of CO2 geological sequestration on the nucleation of earthquakes. *Geophys Res Lett*. 2011;38:L17313. https://doi.org/10.1029/2011GL047974.
11. Chang KW, Segall P. Injection-induced seismicity on basement faults including poroelastic stressing. *J Geophys Res Solid Earth*. 2016;121:2708–2726.
12. Ge S, Saar MO. Induced seismicity during geoenergy development, A hydromechanical perspective. *J Geophys Res Solid Earth*. 2022;127. e2021JB023141.
13. Segall P, Lu S. Injection-induced seismicity: Poroelastic and earthquake nucleation effects. *J Geophys Res Solid Earth*. 2015;120:5082–5103.
14. Vilarrasa V, Carrera J, Olivella S. Hydromechanical characterization of CO2 injection sites. *Int J Greenh Gas Control*. 2013;19:665–677.
15. Zhang Y, Li Q, Tan Y, Li X, Zhong Y. Decomposing significant factors of Coulomb stress and its components in injection-induced seismicity. *J Rock Mech Geotech Eng*. 2024;16:4895–4908.
16. Chang KW, Yoon H, Kim Y, Lee MY. Operational and geological controls of coupled poroelastic stressing and pore-pressure accumulation along faults: Induced earthquakes in Pohang, South Korea. *Sci Rep*. 2020;10:2073.
17. Yang Y, Yang H, Zi J. Stress transfer outpaces injection-induced aseismic slip and triggers seismicity. *Sci Rep*. 2023;13:16626.
18. Dieterich J. A constitutive law for rate of earthquake production and its application to earthquake clustering. *J Geophys Res Solid Earth*. 1994;99:2601–2618.
19. Heimisson ER, Segall P. Constitutive law for earthquake production based on rate-and-state friction: Dieterich 1994 revisited. *J Geophys Res Solid Earth*. 2018;123:4141–4156.
20. Norbeck J, Rubinstein JL. Hydromechanical earthquake nucleation model forecasts onset, peak, and falling rates of induced seismicity in Oklahoma and Kansas. *Geophys Res Lett*. 2018;45:2963–2975.
21. Barton N, Choubey V. The shear strength of rock joints in theory and practice. *Rock Mech*. 1977;10:1–54.
22. Bandis SC, Lumsden AC, Barton NR. Fundamentals of rock joint deformation. *Int J Rock Mech Min Sci Geomech Abstr*. 1983;20:249–268.
23. Laubach SE, Eichhubl P, Hilgers C, Lander RH. Structural diagenesis. *J Struct Geol*. 2010;32:1866–1872.
24. Guglielmi Y, Cappa F, Avouac JP, Henry P, Elsworth D. Seismicity triggered by fluid injection–induced aseismic slip. *Science*. 2015;348:1224–1226.
25. Dunham EM. Fluid-driven aseismic fault slip with permeability enhancement and dilatancy. *Philos Trans A Math Phys Eng Sci*. 2024;382, 20230255.
26. Cochran ES, Rubinstein JL, Barbour AJ, Kaven JO. Induced seismicity strategic vision. *US Geol Surv Circ*. 2024;1509. https://doi.org/10.3133/cir1509.
27. Ai SG, Gao K. Simulating hydraulic fracturing dynamics considering dynamic Biot's poroelasticity and coupled plasticity–damage permeability. *Int J Geomech*. 2025;25, 04025019.
28. Biot MA. General theory of three-dimensional consolidation. *J Appl Phys*. 1941;12:155–164.
29. Chan AH, Pastor M, Schrefler BA, Shiomi T, Zienkiewicz OC. *Computational Geomechanics: Theory and Applications*. John Wiley & Sons; 2022.
30. Chang KW, Segall P. Seismicity on basement faults induced by simultaneous fluid injection–extraction. *Pure Appl Geophys*. 2016;173:2621–2636.
31. Lewis RW, Schrefler B. *The Finite Element Method in the Static and Dynamic Deformation and Consolidation of Porous Media*. John Wiley & Sons; 1998.
32. Shalev E, Lyakhovsky V. The processes controlling damage zone propagation induced by wellbore fluid injection. *Geophys J Int*. 2013;193:209–219.
33. Jaeger JC, Cook NG, Zimmerman R. *Fundamentals of Rock Mechanics*. John Wiley & Sons; 2009.
34. Tsitouras C. Runge–Kutta pairs of order 5 (4) satisfying only the first column simplifying assumption. *Comput Math Appl*. 2011;62:770–775.

35. Ferronato M, Castelletto N, Gambolati G. A fully coupled 3-D mixed finite element model of Biot consolidation. *J Comput Phys*. 2010;229:4813–4830.
36. Guo L, Vardakis JC, Chou D, Ventikos Y. A multiple-network poroelastic model for biological systems and application to subject-specific modelling of cerebral fluid transport. *Int J Eng Sci*. 2020;147, 103204.
37. Bommer JJ, Oates S, Cepeda JM, et al. Control of hazard due to seismicity induced by a hot fractured rock geothermal project. *Eng Geol*. 2006;83:287–306.